The Astrophysical Journal, 849:11 (25pp), 2017 November 1 https://doi.org/10.3847/1538-4357/aa84b3

New Low-mass Eclipsing Binary Systems in Praesepe Discovered by *K2*

Edward Gillen[1], Lynne A. Hillenbrand[2], Trevor J. David[2], Suzanne Aigrain[3], Luisa Rebull[4], John Stauffer[4], Ann Marie Cody[5], and Didier Queloz[1]
[1] Astrophysics Group, Cavendish Laboratory, J.J. Thomson Avenue, Cambridge CB3 0HE, UK; ecg41@cam.ac.uk
[2] Department of Astronomy, California Institute of Technology, Pasadena, CA 91125, USA
[3] Sub-department of Astrophysics, Department of Physics, University of Oxford, Keble Road, Oxford, OX1 3RH, UK
[4] Spitzer Science Center, California Institute of Technology, 1200 E California Blvd., Pasadena, CA 91125, USA
[5] NASA Ames Research Center, Moffet Field, CA 94035, USA
Received 2017 April 4; revised 2017 June 7; accepted 2017 June 8; published 2017 October 24

Abstract

We present the discovery and characterization of four low-mass ($M < 0.6\ M_{\odot}$) eclipsing binary (EB) systems in the sub-Gyr old Praesepe open cluster using *Kepler*/*K2* time series photometry and Keck/HIRES spectroscopy. We present a new Gaussian process EB model, GP–EBOP, as well as a method of simultaneously determining effective temperatures and distances for EBs. Three of the reported systems (AD 3814, AD 2615 and AD 1508) are detached and double-lined, and precise solutions are presented for the first two. We determine masses and radii to 1%–3% precision for AD 3814 and to 5%–6% for AD 2615. Together with effective temperatures determined to ∼50 K precision, we test the PARSEC v1.2 and BHAC15 stellar evolution models. Our EB parameters are more consistent with the PARSEC models, primarily because the BHAC15 temperature scale is hotter than our data over the mid-M-dwarf mass range probed. Both ADs 3814 and 2615, which have orbital periods of 6.0 and 11.6 days, are circularized but not synchronized. This suggests that either synchronization proceeds more slowly in fully convective stars than the theory of equilibrium tides predicts, or magnetic braking is currently playing a more important role than tidal forces in the spin evolution of these binaries. The fourth system (AD 3116) comprises a brown dwarf transiting a mid-M-dwarf, which is the first such system discovered in a sub-Gyr open cluster. Finally, these new discoveries increase the number of characterized EBs in sub-Gyr open clusters by 20% (40%) below $M < 1.5\ M_{\odot}$ ($M < 0.6\ M_{\odot}$).

Key words: binaries: eclipsing – binaries: spectroscopic – brown dwarfs – stars: evolution – stars: fundamental parameters – stars: low-mass

1. Introduction

Stellar evolution theory underpins much of observational astrophysics, yet significant uncertainties remain at low masses ($M \lesssim 0.8\ M_{\odot}$) and young ages ($t \lesssim 1$ Gyr). Unfortunately, this mass and age range is also where observational constraints are scarce. The fundamental goal of stellar evolution theory is to accurately predict the observables (radius, temperature, and luminosity) for a star of given mass, age, and metallicity. The evolutionary pathway of a star is governed primarily by its mass, which is accessible only through the study of gravitational interactions such as in binary or higher-order multiple-star systems. For eclipsing binaries (EBs), the ratio of the radii of the stars is attainable. EBs are particularly important objects if they are also detected as double-lined systems in spectra, as the individual masses and radii of both stars can be extracted from the combined light curves and radial velocity (RV) curves of the system. Radii can also be measured directly using interferometric techniques, but only for the brightest of nearby stars. When the inferred mass and radius values reach a precision of a few percent or less, they provide one of the strongest observational tests of stellar evolution theory available (e.g., Torres et al. 2010; Stassun et al. 2014).

Open clusters are fruitful astrophysical laboratories, given that their members share broad coevality, composition, and distance. The detection of multiple EBs in a given cluster, with each member of each pair sharing the same age and metallicity but spanning a range of masses, offers a particularly strong test of stellar evolution theory. The pursuit of EB parameters, among other science goals, has motivated numerous programs to target open clusters via time series photometry, e.g., the ground-based Monitor, PTF Orion, and YETI projects (Aigrain et al. 2007; van Eyken et al. 2011; Neuhäuser et al. 2011), and space-based observations with *CoRoT* and *Spitzer* (Gillen et al. 2014; Morales-Calderón et al. 2012). Furthermore, since 2014 March, the repurposed *Kepler* mission, *K2* (Howell et al. 2014), has targeted a number of star-forming regions and young (sub-Gyr) open clusters across the ecliptic for ∼80 days each. To date, the nearby ρ Ophiuchi star-forming region and Upper Scorpius young OB association (∼1 and 5–10 Myr, respectively) were observed in Campaign 2, as were the Pleiades and Hyades open clusters (∼125, 600–800 Myr, respectively) in Campaign 4 and Praesepe (600–800 Myr) in Campaign 5.

The Praesepe open cluster, also known as the Beehive cluster or M44, was targeted by *K2* in Campaign 5 (2015 April–July). Praesepe is a relatively nearby, metal-rich, several hundred Myr cluster hosting >1000 high-probability members (>80%) and more than 100 candidate members (>50% probability; Kraus & Hillenbrand 2007; Rebull et al. 2017). Given its richness and proximity, Praesepe is a well-studied benchmark cluster. The parallaxes of bright Praesepe members in the *Gaia* DR1 suggest a distance of $182.8 \pm 1.7 \pm 14$ pc, where the first error represents the uncertainty on the cluster center determination and the second reflects the observed radial spread of high-probability members on the sky (Gaia Collaboration et al. 2017). This is in agreement with the commonly quoted *Hipparcos* distance to the cluster, 181.5 ± 6.0 pc (van Leeuwen 2009). The cluster has a low reddening along the

line of sight of $E(B-V) = 0.027 \pm 0.004$ (Taylor 2006). Metallicity estimates typically fall within the range [Fe/H] ~0.12–0.16 (e.g., Boesgaard et al. 2013; Yang et al. 2015; Netopil et al. 2016), but can be as high as [Fe/H] = 0.27 ± 0.10 (e.g., Pace et al. 2008). The age of Praesepe is estimated to be in the range ~600–900 Myr (e.g., Adams et al. 2002) with traditional estimates typically falling at the lower end, often through association with the Hyades (e.g., Salaris et al. 2004). More recently, however, Brandt & Huang (2015b) included stellar rotation to conclude that the upper main sequences of both Praesepe and the Hyades were consistently well-fit at an age of ~750–800 Myr. The age of Praesepe is further discussed in Section 6.2.3.

The binary fraction within the cluster has been extensively studied. Pinfield et al. (2003) noted that binaries in Praesepe appear to favor similar-mass systems. Boudreault et al. (2012) focused on the low-mass population, finding binary frequencies of 25.6% ± 3.0% between $0.2 < M < 0.45\ M_{\odot}$, 19.6% ± 3.0% between $0.1 < M < 0.2\ M_{\odot}$ and 23.2% ± 5.6% between $0.07 < M < 0.1\ M_{\odot}$. Wang et al. (2014) analyzed the full Praesepe membership to find a binary occurrence rate of 20%–40%. Furthermore, a significant population of binaries and higher-order systems were identified by Khalaj & Baumgardt (2013), who propose a binary fraction of 35% ± 5% in the mass range 0.6–2.2 $M_{\odot}$, assuming mass-dependent pairing of primary stars following the results of recent star formation simulations (e.g., Bate 2009).

This paper presents the characterization of four high-probability, low-mass EB members of Praesepe. Section 2 describes the sources and previous literature characterization. In Section 3, we detail the photometric and spectroscopic observations. In Section 4, we present a modified EB model for detached systems, GP–EBOP, and describe the light curve and radial velocity (RV) analyses. We then present the results for each system in Section 5. In Section 6, we present an updated method to simultaneously determine the effective temperatures of both stars as well as the distance to an EB system, before discussing these new EBs in the context of calibrating stellar evolution models, and informing tidal evolution theory in close binaries. Finally, we conclude in Section 7.

2. New EBs Among Praesepe Members

Half a dozen deep proper motion surveys of Praesepe have been published since 2000 (Adams et al. 2002; Kraus & Hillenbrand 2007; Baker et al. 2010; Boudreault et al. 2012; Khalaj & Baumgardt 2013; Wang et al. 2014). Three of our four EBs are considered Praesepe members in at least four of those six studies (AD 3814, 2615, and 3116). Our fourth EB (AD 1508) is identified as a Praesepe member in only two of those studies.

In the top panel of Figure 1, we show where these four objects fall on a V versus V–K_s color–magnitude diagram, where we have derived V–K_s estimates based on a conversion (Rebull et al. 2017) from G–K_s, where G is the star's magnitude in the *Gaia* DR1 catalog. All four stars have photometry consistent with Praesepe membership. AD 1508 has the earliest type (brightest) of the four; it is located well above the single star main-sequence locus, suggesting that it is a nearly equal-mass binary. ADs 3116 and 3814 are located nearly on the single star main-sequence locus, and so their binary companions are presumably very low mass. AD 2615 is displaced about 0.4 mag above the single star locus, and so is likely to have an intermediate-mass binary companion.

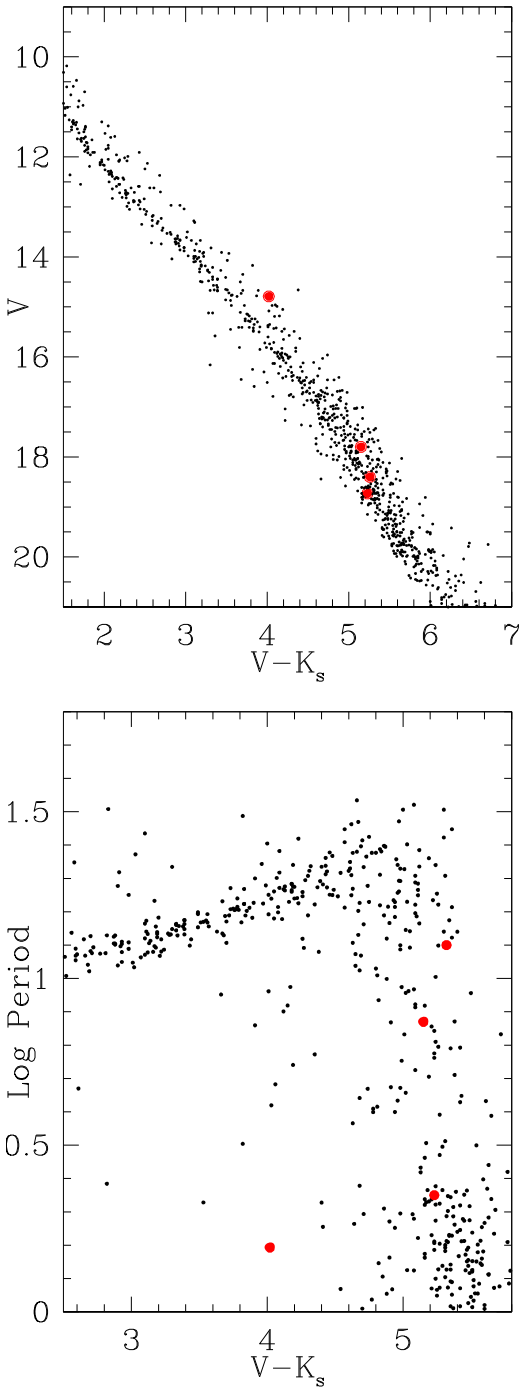

Figure 1. Color–magnitude diagram (top) and color–rotation period diagram (bottom) illustrating the location of the four new eclipsing systems relative to the sequence of Praesepe members. Top: from brightest to faintest, AD 1508, AD 3814, AD 2615, and AD 3116, with elevation above the color–magnitude sequence a rough indicator of the mass ratio of a binary system (equal-mass ratio produces a 0.75 mag magnitude excess). Bottom: from slowest to fastest rotators, AD 2615, AD 3814, AD 3116 and AD 1508.

Three of the four stars have published spectral types: AD 3814—M5 (West et al. 2011); AD 2615—M4.0 (Adams et al. 2002) and M5 (West et al. 2011); and AD 3116—M4.5 (Adams et al. 2002) and M3.9 (Kafka & Honeycutt 2006). These spectral types are broadly consistent with their V–K_s colors. All four systems have spectral types estimated from photometry (Kraus & Hillenbrand 2007): AD 3814—M3.4 ± 0.1; AD 2615—M4.0 ± 0.1; AD 3116—M3.9 ± 0.1;

Table 1
Names, Coordinates, Properties, and Membership Information for the Four Newly Identified EBs

Property	Units	AD 3814	AD 2615	AD 3116	AD 1508	References
EPIC		211972086	212002525	211946007	212009427	⋯
2MASS		J08504984+1948364	J08394203+2017450	J08423943+1924520	J08312987+2024374	⋯
Other names		⋯	⋯	HSHJ 430	⋯	(1)
R.A.	J2000.0	08:50:49.84	08:39:42.03	08:42:39.43	08:31:29.87	⋯
Decl.	J2000.0	+19:48:36.4	+20:17:45.0	+19:24:51.9	+20:24:37.5	⋯
u	AB	21.009 ± 0.093	21.747 ± 0.185	22.290 ± 0.190	18.102 ± 0.014	(2)
g	AB	18.769 ± 0.008	19.416 ± 0.012	19.646 ± 0.014	15.540 ± 0.004	(2)
r	AB	17.299 ± 0.006	17.905 ± 0.007	18.206 ± 0.007	14.151 ± 0.004	(2)
i	AB	15.803 ± 0.005	16.324 ± 0.004	16.675 ± 0.005	13.700 ± 0.001	(2)
z	AB	14.999 ± 0.005	15.456 ± 0.006	15.845 ± 0.006	12.905 ± 0.004	(2)
V	Vega	17.80	18.46	18.73	14.79	(3)
J	Vega	13.529 ± 0.026	14.027 ± 0.021	14.348 ± 0.032	11.674 ± 0.022	(4)
H	Vega	12.911 ± 0.024	13.456 ± 0.026	13.769 ± 0.037	10.949 ± 0.023	(4)
K_s	Vega	12.651 ± 0.022	13.136 ± 0.034	13.499 ± 0.043	10.767 ± 0.020	(4)
WISE 1	Vega	12.478 ± 0.024	12.938 ± 0.024	13.299 ± 0.029	10.677 ± 0.023	(4)
WISE 2	Vega	12.291 ± 0.026	12.773 ± 0.031	13.096 ± 0.039	10.638 ± 0.021	(4)
Spectral type	M subtype	3.4 ± 0.1	4.0 ± 0.1	3.9 ± 0.3	0.1 ± 0.1	(5)
Hα emission	Å	2.4–3.5, ⋯	3.0–4.3, 10.7	3.1–5.2, 4.6	2.0–2.1, ⋯	(6), (7)
R.A. proper motion, μ_α	mas yr^{-1}	−37.5	−39.3	−37.5	−37.3	(5)
Decl. proper motion, μ_δ	mas yr^{-1}	−14.1	−11.6	−8.2	−16.7	(5)
Membership probability	%	97.9	99.7	99.1	98.3	(5)

Note. The quoted photometric uncertainties are formal measurement errors and hence do not capture the intrinsic variability of these systems.
References. (1) Hambly et al. (1995); (2) Sloan Digital Sky Survey Data Release 13; (3) Rebull et al. (2017); (4) NASA/IPAC Infrared Science Archive; (5) Kraus & Hillenbrand (2007); (6) this work, with quoted range as measured over the epochs listed in Table 2; (7) Adams et al. (2002).

and AD 1508—M0.1 ± 0.1. As these form a homogeneous set for our EBs, we adopt these spectral types here. For each system, properties extracted from the literature are reported in Table 1.

In the bottom panel of Figure 1, we show the Praesepe V versus V–K_s color versus rotation period diagram, and indicate our four systems in red. Given the wide spread in rotation periods for mid-M-dwarfs, ADs 3814, 2615, and 3116 all lie along the single star trend, but the early M-dwarf AD 1508 lies far below the single star trend with a short rotation period.

3. Observations

3.1. Photometry

We proposed targets for the *K2* Campaign 5 observations, which included Praesepe, as part of the *K2* Young Suns Survey (PI Stauffer). Targets were collated through merging various proper motion surveys (Klein Wassink 1927; Jones & Cudworth 1983; Jones & Stauffer 1991; Kraus & Hillenbrand 2007; Wang et al. 2014) with published *BVRI* photometry (Stauffer 1982; Mermilliod et al. 1990; and references therein). The K2FOV tool was used to select targets falling "on silicon," and we further limited our proposal to stars with spectral type later than F0 (i.e., possessing outer convective envelopes) and brighter than $R < 17$. This gave 477 high-probability Praesepe targets in total. In addition to our proposed systems, we also investigated the light curves of Praesepe candidates from other *K2* programs.

The *K2* observations of Praesepe spanned 2015 April 27–July 10, and the FoV was centered on 08:40:38+16:49:47. Given the typical 30 minute cadence of *Kepler* observations, this resulted in ∼3300 data points for each target. Short cadence (1 minute) observations are also possible for a small number of targets but all systems presented here were observed in standard long cadence mode. We discuss our method to reduce the *K2* photometry in Section 3.1.1. For objects showing the signatures of eclipses in the *K2* time series photometry, we cross-referenced the EPIC identifiers with literature information in order to determine basic system properties (see Section 3.1.2) and to identify which systems to pursue with high-dispersion spectroscopy (see Section 3.2).

3.1.1. K2 Data Detrending and Eclipse Detection

We started from the Simple Aperture Photometry (SAP) light curves, which were made available at the Mikulski Archive for Space Telescopes (MAST) as part of *K2* Data Release 7.[6] We used the K2SC pipeline (Aigrain et al. 2016) to correct the light curves for systematics caused by the quasi-periodic rolling motion of the spacecraft, while preserving the intrinsic variability of the target stars. K2SC works by modeling the SAP flux as the sum of two smooth, random functions: one depending on the star's position on the detector, and one depending on time, plus white noise. The position component represents instrumental systematics associated with the satellite's pointing variations (mainly intra- and inter-pixel sensitivity variations), while the time component represents the star's intrinsic variability, plus any long-term instrumental effects not accounted for by the position component. Both components are modeled using Gaussian Process (GP) regression (see Section 4.1 for further details and references on GPs). While both components are initially treated as aperiodic, a quasi-periodic GP is automatically used for the time component if the light curve shows any evidence of

[6] See https://keplerscience.arc.nasa.gov/k2-data-release-notes.html#k2-campaign-5 for details.

periodic behavior after a first pass treatment with default parameters.

A careful treatment of outliers ensures that K2SC mostly preserves short-duration events such as planetary transits or stellar eclipses. However, once the eclipses were identified (by visual examination) in the four systems discussed in the present paper, their light curves were re-processed using K2SC's periodic mask option. This option enables the user to supply the period, epoch, and duration of the eclipses, and any in-eclipse points are then ignored when training the GP model. In effect, we are using the K2SC GP model to interpolate in both flux and position space to the times affected by the eclipses, thereby providing a model prediction for the total system flux across each eclipse. In our analysis, we use the K2SC light curve that has been detrended for instrument systematics but which retains the stellar variability component. This allows us to simultaneously model both the stellar variability and eclipses (see Section 4).

3.1.2. Estimation of Primary Star Properties from Broadband Colors

We estimated primary star effective temperatures and masses using broadband color relations and the absolute magnitudes presented in Table 1, respectively.

Effective temperatures ($T_{\rm eff}$) were estimated using the empirical color–$T_{\rm eff}$ relations presented in Mann et al. (2015; their Equation (6)) and David et al. (2016a; their Equation (1), which is derived from fitting polynomials to the color and temperature data presented in Pecaut & Mamajek 2013 for dwarf stars, and is valid for $0.3 < V - K_s < 7.0$). These predict primary effective temperatures of ∼3250, 3190, 3240, and 3750 K for ADs 3814, 2615, 3116, and 1508, respectively. In Section 6.1, we directly determine the effective temperatures of both stars in each EB by modeling their spectral energy distributions (SEDs) and compare our $T_{\rm eff}$ values to these empirical predictions in Table 4.

We estimated primary masses from absolute K-band magnitudes using the semi-empirical relation of Mann et al. (2015; their Equation (10)) and the empirical relation of Benedict et al. (2016; their Equation (11)). For this, we converted apparent to absolute magnitudes assuming a cluster distance of 182.8 ± 14 pc (Gaia Collaboration et al. 2017) and assumed a reddening along the line of sight of $E(B - V) = 0.027 \pm 0.004$ (Taylor 2006). These two relations predict primary masses of ∼0.43, 0.34, 0.28, and 0.72 $M_\odot$ for ADs 3814, 2615, 3116, and 1508, respectively. For AD 1508, we used only the Mann et al. (2015) mass prediction as this system lies outside the validity range ($0.1 \lesssim M \lesssim 0.6\ M_\odot$) of the Benedict relation.

We note that these predictions are for single stars and hence are not appropriate for binary systems unless the system magnitudes are dominated by the primary component. Furthermore, these empirical relations are approximations only and are estimated from systems that typically do not contain as high a metallicity as Praesepe ([Fe/H] ∼ 0.1–0.27). Nonetheless, they serve to highlight the expected temperature and mass regimes of the systems to be analyzed.

3.2. Spectroscopy

We obtained high-resolution spectra for each of the identified EB systems using the Keck HIRES spectrograph (Vogt et al. 1994). The observations were taken between 2015 December and 2017 January, with the exact epochs along with the estimated signal-to-noise ratios (S/Ns) and measured radial velocities given in Table 2. The spectra cover the wavelength range ≈4800–9200 Å at a spectral resolution of $R > 36{,}000$ and were reduced using the *makee* software written by Tom Barlow. We measured radial velocities using the cross-correlation techniques within the *fxcor* task in *IRAF*, with absolute reference to between three and five (depending on the night) late-type RV standards. The standards and their approximate spectral types include GJ 514 (M0.5), HD 95650 (M1), LHS 3433B (M2), Gl 821 (M2), GJ 408 (M2.5), GJ 176 (M2.5), GJ 109 (M3.5), GJ 402 (M4), Gl 876 (M4), GJ 105B (M4.5), GJ 388 (M4.5), GJ411 (M4.5), and GJ 406 (M6.5), with the reference velocities generally taken from Nidever et al. (2002). Telluric-free spectral regions were selected over between 6 and 19 orders (depending on the S/N of the target spectrum) for cross-correlation function fitting. Depending on the velocity separation of the peaks, they were fit either singly or simultaneously, and depending on the S/N of the spectrum, the fitting function was either Gaussian or parabolic. Errors in the quoted radial velocities were determined from the empirical scatter among the measured orders and reference stars for each observation, with some hand editing to remove extreme outliers deriving from particularly poor measurements. In general, the scatter among the measurements that is quoted as the RV error is smaller than or comparable to the mean among the errors in the individual measurements over the orders and reference stars included in the quoted RV value. This gives us some confidence that we are accurately representing the random errors in our methods.

AD 3814, AD 2615, and AD 1508 are detected as double-lined systems, with measurable radial velocities for each component at nearly all epochs. AD 3116, however, presented only a single-line set, which we attribute to the primary. In the double-lined systems, the CCF peak height ratios were used to approximate the light ratio between the two components, which was then applied as a prior in the light curve modeling (see Section 4).

In addition to the radial velocities, Hα equivalent width measurements were made for each EB using the *splot* task in IRAF. The values quoted in Table 1 represent the combined system, and the range records the variability over the various epochs of observation in Table 2.

4. Analysis with the GP–EBOP Model

Both young and low-mass stars typically display photometric and spectroscopic modulation arising from the longitudinal inhomogeneity of active regions on the stellar surface, with activity timescales a strong function of stellar mass. In close binaries ($P \lesssim 15$ days), activity levels are generally observed to be higher than in their single star counterparts. This variability is important to properly account for when analyzing the observed stellar eclipses since it can subtly modify the detailed shape of individual eclipses. Ideally, therefore, we would model the stellar variability at the same time as fitting for the eclipses and, in doing so, propagate any uncertainties in the variability modeling in through to the posterior distributions for the EB parameters. This approach motivated the development of a new EB model, GP–EBOP, which we use here to characterize the new Praesepe EBs by simultaneously modeling the *K2* light curves and Keck/HIRES RV measurements, accounting for activity-induced effects. The method is distinct

Table 2
Radial Velocities Derived from Keck/HIRES Spectra for ADs 3814, 2615, 3116, and 1508

Epoch			S/N	RV (km s^{-1})	
UT date	BJD	Phase [a]	7500 Å	Primary	Secondary
			AD 3814		
2015 Dec 24	2457381.15090	0.607	16	54.08 ± 0.77	−6.83 ± 0.93
2015 Dec 29	2457386.14539	0.437	16	21.42 ± 0.76	58.70 ± 1.10
2016 Feb 02	2457420.89940	0.214	16	0.10 ± 0.75	95.82 ± 1.13
2016 Feb 03	2457421.92652	0.385	15	12.91 ± 0.76	77.18 ± 0.93
2016 May 17	2457525.80479	0.652	14	60.96 ± 0.37	−19.29 ± 1.15
2016 Dec 22	2457744.96970	0.084	15	15.72 ± 0.35	65.38 ± 0.56
2016 Dec 26	2457748.97551	0.750	13	68.56 ± 1.04	−28.91 ± 1.18
2017 Jan 13	2457766.85771	0.723	12	67.17 ± 0.40	−29.35 ± 0.56
			AD 2615		
2015 Dec 29	2457386.16741	0.039	13	26.03 ± 0.86	43.50 ± 0.77
2016 May 17	2457525.78402	0.059	13	20.45 ± 0.76	45.69 ± 0.80
2016 May 20	2457528.78074	0.317	14	−1.28 ± 0.60	65.74 ± 0.60
2016 Oct 14	2457676.07100	0.997	10	35.22 ± 0.29	
2016 Dec 22	2457745.03382	0.935	13	49.63 ± 0.48	20.66 ± 0.41
2017 Jan 13	2457766.90914	0.818	5	72.09 ± 0.53	5.63 ± 0.60
			AD 3116		
2016 Feb 02	2457420.92116	0.102	12	26.28 ± 0.82	⋯
2016 Feb 03	2457421.90606	0.599	12	40.47 ± 0.83	⋯
2016 May 17	2457525.76250	0.978	12	39.75 ± 0.59	⋯
2016 May 20	2457528.75747	0.488	13	27.46 ± 0.54	⋯
2016 Oct 14	2457676.09435	0.796	13	55.96 ± 0.30	⋯
2016 Dec 22	2457744.98886	0.542	12	31.91 ± 0.44	⋯
2017 Jan 13	2457766.87986	0.583	6	37.23 ± 0.77	⋯
			AD 1508		
2016 Dec 22	2457745.04753	0.971	40	50.62 ± 1.40	16.36 ± 1.57
2016 Dec 26	2457748.95332	0.479	30	21.66 ± 2.79	42.37 ± 3.23
2017 Jan 13	2457766.84264	0.970	40	52.56 ± 2.19	18.69 ± 1.82

Note.
[a] Phase is defined relative to primary eclipse.

from those that account for stellar variability by detrending first and then modeling eclipses second.

4.1. GP–EBOP

GP–EBOP comprises a central EB (EBOP) model coupled with a Gaussian process (GP) model, which has an MCMC (Markov Chain Monte Carlo) wrapper. It can be used to model both EB systems and transiting planets: we use it here in its first capacity but note its tested ability to model planet transits (e.g., Pepper et al. 2017). Below we briefly describe the main components of the model.

1. *EB component*. The EB model is a modified version of the (JKT)EBOP family of models, which was first presented in Irwin et al. (2011). Each star is modeled as a sphere when computing light curves from the eclipses and as a biaxial spheroid when calculating reflection and ellipsoidal effects. This model is able to compute light ratios and radial velocities, and can correct for the "classical" light travel time across the system.

   Different from previous EBOP-based models, this implementation uses the analytic method of Mandel & Agol (2002) for the quadratic limb-darkening law. GP–EBOP utilizes the LDtk toolkit (Parviainen & Aigrain 2015), which allows uncertainties in the stellar parameters (effective temperature, surface gravity, and metallicity) to be propagated through the PHOENIX stellar atmosphere models (Husser et al. 2013) and into priors on the limb-darkening coefficients. Limb-darkening parameterization within the fitting process follows the triangular sampling method of Kipping (2013).
2. *GP component*. The GP model utilizes the `george` package[7] (Ambikasaran et al. 2014) and is used to model the out-of-eclipse (OOE) photometric data. A detailed description of GP regression is beyond the scope of this paper but the interested reader is referred to Roberts et al. (2012) for a gentle introduction, Rasmussen & Williams (2006) for a more detailed entry, Aigrain et al. (2012) for application to stellar light curves, and Gillen et al. (2014) for application to EB light curves and cross-correlation functions.

   A simple way to view GPs is to think of them as a means of modeling a light curve by parameterizing the covariance between pairs of flux measurements, rather than explicitly specifying a functional form of model to fit the data. In this GP model, the joint distribution of the

[7] http://dan.iel.fm/george

observed flux measurements is taken to be a multivariate Gaussian, whose covariance matrix is populated through a covariance function that depends on the observation times. As such, a GP is a distribution over functions. When the parameters of a GP (called hyperparameters) are varied, we step through function space rather than the more familiar parameter space of conventional methods.

Crucially for our application, the power of GP regression is that we obtain an uncertainty on the prediction for the OOE variability across each eclipse, which we can then propagate into our posterior distributions for the EB parameters.

3. *MCMC wrapper*. GP–EBOP explores the posterior parameter space using the affine invariant MCMC method, as implemented in `emcee` (Foreman-Mackey et al. 2013).

4.2. Light Curves

The *K*2 light curves are a time series of flux measurements. GP–EBOP models the light curves by assuming that the joint distribution over the flux measurements $\boldsymbol{F}$ is given by a multivariate Gaussian whose mean function μ is an eclipse model and whose covariance matrix $\boldsymbol{K}$ is described by a GP:

$$\boldsymbol{F} \sim \mathcal{N}(\mu, \boldsymbol{K}). \quad (1)$$

The elements of the covariance matrix $\boldsymbol{K}$ are given by

$$\boldsymbol{K}_{ij} = k(t_i, t_j) + k_w(i, j), \quad (2)$$

where the first term represents the specific kernel chosen to describe the OOE variations and the second term describes the white noise component.

Figure 2 shows the raw light curves of the four new EBs, and Figure 3 shows these phase-folded on the photometric variability period. The OOE light curves of all four systems presented here display evolving starspot modulation with characteristic amplitudes, periods, and evolutionary timescales. To model these smoothly evolving data, therefore, we chose a GP with a quasi-periodic Exponential Sine-Squared kernel (hereafter QPESS). This is a periodic kernel that is allowed to evolve over time, i.e., mimicking evolving starspot modulation. The QPESS kernel has the required flexibility to explain the large-scale flux variations in the OOE light curves. It is given by

$$k_{\mathrm{QPESS}}(t_i, t_j) = A^2 \exp\left[-\Gamma \sin^2\left(\frac{\pi|t_i - t_j|}{P}\right) - \frac{(t_i - t_j)^2}{2l^2}\right]. \quad (3)$$

The first exponential describes the periodic component and the second the evolution of the periodic signal. A is the characteristic amplitude of the variations, Γ is the scale of the correlations, P is the period of the oscillations, and l is the evolutionary timescale. t_i and t_j represent example times of two flux measurements within the time series. The resulting periods (Table 6) differ from those reported by Rebull et al. (2017; based on Lomb–Scargle techniques) at about the $\sim$1% level. The white noise term is given by

$$k_w(i, j) = \sigma^2 \delta_{ij}, \quad (4)$$

where σ is the standard deviation and δ_{ij} is the Kronecker delta function. Within GP–EBOP, the white noise term is incorporated via a multiplicative scale factor on the observational uncertainties, as `george` adds these scaled uncertainties in quadrature to the diagonal of the covariance matrix.

We model the K2SC light curves that have been detrended for instrument systematics but which still contain stellar activity variations. After visual inspection of the SAP and PDC K2SC light curves, we opted to work with the PDC versions as these display lower point-to-point scatter.

As can be seen in Figure 2, numerous stellar flares are present throughout the light curves. Flares were treated in two ways depending on whether or not they affected the stellar eclipses. Those that did not were automatically removed using the following method: the light curve was smoothed using a running median filter, which was followed by running sigma cuts to identify flares. The data before and after the flare peak was removed until the light curve returned to the smoothed light curve value. Flares affecting the stellar eclipses were treated more carefully: as even a detailed modeling would not correct the photometry to a precision required to include in our eclipse modeling, we opted to conservatively mask out the affected data via visual inspection. The resulting light curves, which were modeled in our analyses of ADs 3814, 2615 and 3116, are discussed in Section 5 (see Figure 4 as an example for AD 3814). The light curve of AD 1508 was treated slightly differently as only a preliminary solution is presented here (see Section 5.4 for details).

The full light curves (eclipses and OOE variability) and RV variations were simultaneously modeled by GP–EBOP stepping through the parameter space 50,000 times with each of the 144 "walkers." The first 25,000 steps were discarded as burn-in and the remainder of each chain was thinned following inspection of the autocorrelation lengths for each parameter. To account for the $\sim$30 minute cadence of *K2* observations, GP–EBOP was supersampled at 1 minute cadence and numerically integrated to the *K2* sampling for model evaluation. The uncertainties on the limb-darkening coefficients were inflated by a factor of 30, above the uncertainties derived from the PHOENIX models. This inflation factor was determined by comparing the quadratic limb-darkening coefficients of LDtk, Claret et al. (2012), and Sing (2010) for common T_{eff}, $\log g$, and metallicity values in a representative range for our EBs across the *Kepler* bandpass. We used the spread in their predictions, and applied a further increase to account for systematic uncertainties in M-dwarf model atmospheres, to determine our inflation factor. Reflection effects and gravity brightening were not included in the modeling. The former is accounted for by the GP model and the latter makes no significant difference to the model posterior distributions, which we tested by performing model runs with different gravity-brightening exponent (β) values. We note that Alencar & Vaz (1997) found that β ranges between 0.2 and 0.4 for stars with temperatures between $3700 \leqslant T \leqslant 7000$ K and that the typical Lucy (1967) value of $\beta = 0.32$ best describes stars with $T = 6500$ K.

4.3. Radial Velocities

The Keck/HIRES RVs were modeled using Keplerian orbits simultaneously with the *K2* light curves. Spectroscopic light ratios (available for three of the four systems presented here) were estimated from cross-correlation peak heights and applied as priors on the light curve model component. This can help break the well-known degeneracy between the radius

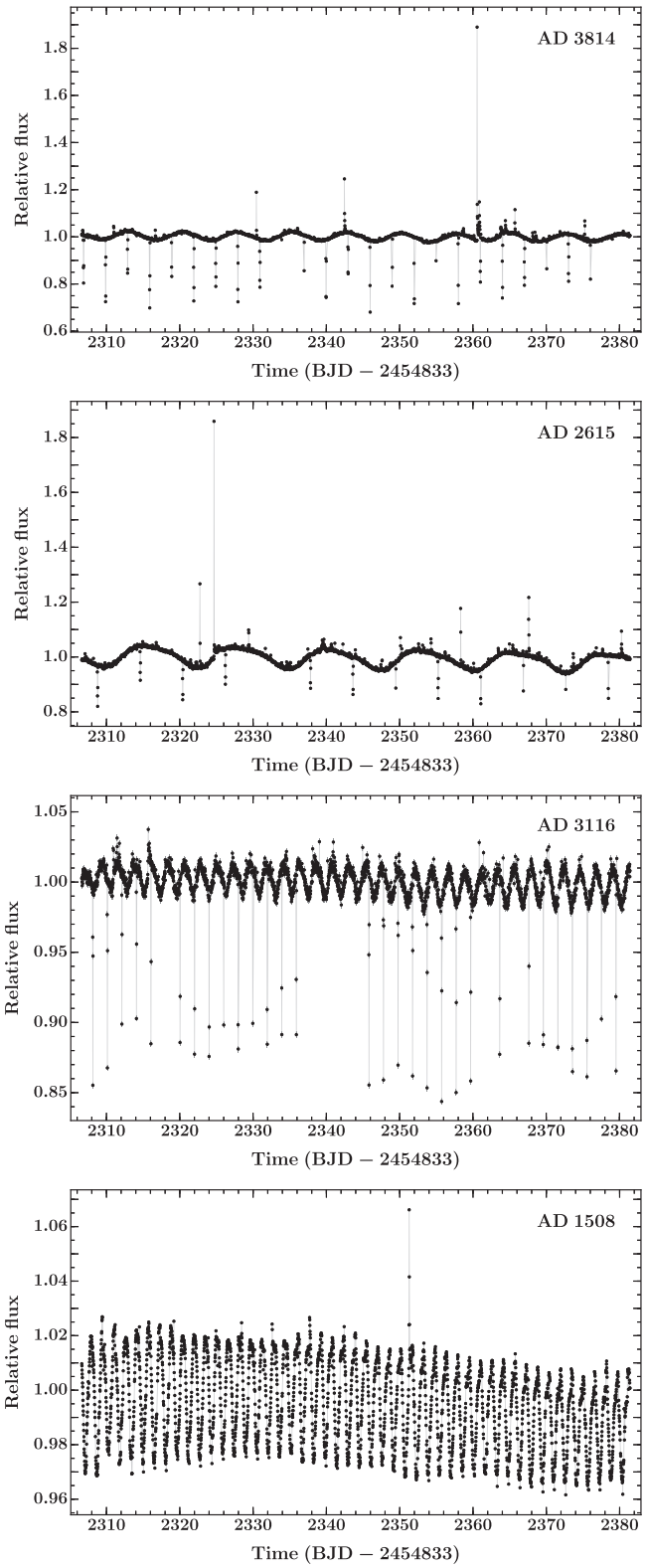

Figure 2. Systematics-detrended K2SC PDC light curves of ADs 3814, 2615, 3116, and 1508 (top to bottom). Each system shows the out-of-eclipse variations arising from evolving starspot modulation upon which the stellar eclipses are superposed. Numerous stellar flares are visible throughout the observations, most notably on ADs 3814 and 2615, including one in each system reaching a relative flux $\gtrsim$1.8. Missing eclipses, as seen in AD 3116, are an artifact present in the PDC light curves.

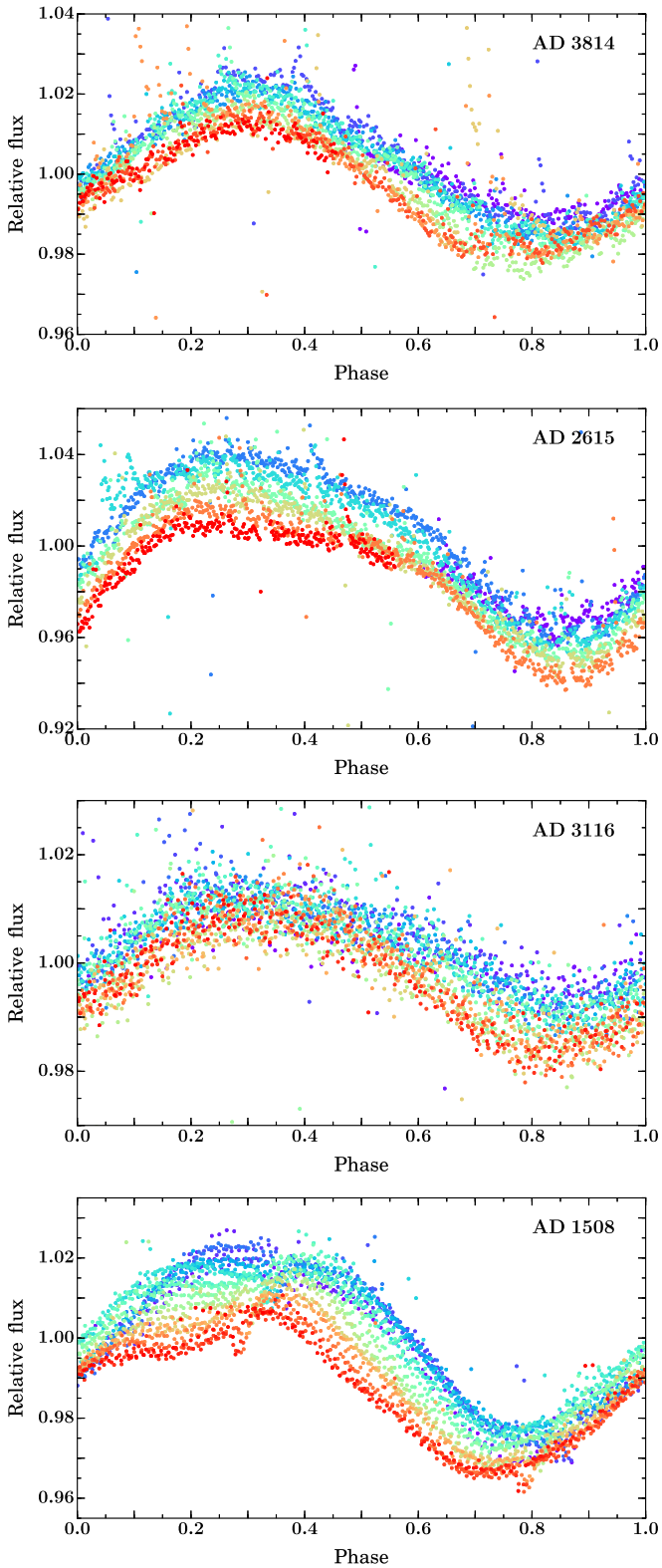

Figure 3. Evolution of the photometric modulation observed in ADs 3814, 2615, 3116, and 1508 (top to bottom). The systematics-detrended K2SC light curves shown in Figure 2 have been folded on the period of the observed variability. The rainbow color scheme highlights the evolution throughout the 75 day campaign (beginning to end, violet to red). For ADs 3814, 2615, 3116, and 1508, the number of periods folded upon is 11, 7, 34, and 49, respectively, which simply reflects the orbital periods of the systems.

and surface brightness ratios, which can often be a limiting factor in the individual radius estimates for near-equal-mass EBs.

An RV jitter term, incorporated in GP–EBOP, was used to allow the uncertainties on the Keck/HIRES RV measurements to be scaled, if necessary. This helps account for additional variations arising from, e.g., stellar activity and instrument systematics. This jitter term is added in quadrature to the observational uncertainties. When RVs from multiple instruments are obtained, GP–EBOP can scale the uncertainties for each instrument individually and account for offsets between different instrument RV zero points.

5. Results

The *K*2 light curves and Keck/HIRES RV measurements of the four new EBs (ADs 3814, 2615, 3116, and 1508) were modeled with GP–EBOP; the results for each system are discussed in turn below. Throughout our analysis, we define the primary as the star that, when occulted, gives the deepest eclipse, and the secondary as the occulting star. We note that these adjectives do not necessarily imply that the primary star is the more massive or brighter star, as we find to be the case with AD 2615.

5.1. AD 3814

AD 3814 has been extensively studied in the literature. The M3.4 spectral type, broadband photometric magnitudes and colors, and proper motion give AD 3814 a high probability of cluster membership. Figure 4 shows the *K2* light curve used in the modeling after flares were removed. Three eclipses were masked in the flare removal process (see Section 4.2): two secondary eclipses at rBJD[8] $\sim$ 2315 and 2361, and one primary eclipse at rBJD $\sim$ 2364. The red line and pink shaded region indicate the mean and 2σ uncertainty of the posterior GP–EBOP eclipse model, which is able to reproduce both the eclipses and the slowly evolving starspot modulation.

Detrending with respect to the GP component and phase-folding on the binary orbital period allows us to inspect the shape of the eclipses in detail. These are shown in Figure 5, where the top panel displays the full phase-folded light curve and the bottom panels show zooms around primary and secondary eclipses (left and right, respectively). There is clear evidence of increased scatter in the residuals across each eclipse, which is presumably due to uncorrected differential starspot effects. Starspots on the background star will have a differential effect on the eclipse shape, with the eclipse being shallower if starspots on the background star are preferentially occulted by the foreground star and deeper if the unspotted photosphere is preferentially occulted. As the timescale for such differential effects are much faster than the typical starspot modulation observed out of eclipse, the QPESS kernel will struggle to account for this effect given its covariance properties, which constrain it to smooth variations. Instead, the GP will opt to inflate its uncertainty due to the increased scatter. One could theoretically include an additional kernel within the GP model to try and account for such differential effects across eclipses, but this is beyond the scope of the current work.

The eight Keck/HIRES RVs were modeled simultaneously with the *K2* light curve. The resulting phase-folded RV orbit is shown in Figure 6 (primary in red and secondary in blue). The colored lines and shaded regions indicate the median and 2σ uncertainties on the posterior orbits of the two stars, which are well-fit to the observed RVs. The systemic velocity of the system is $V_{\rm sys} = 33.60 \pm 0.24$ km s^{-1} (dashed gray line), which is consistent with the recessional velocity of the cluster, $V_{\rm rec} \sim 33$–35 km s^{-1} (e.g., van Leeuwen 2009; Quinn et al. 2012; Yang et al. 2015), and hence provides further evidence of cluster membership. We note that the residuals in the phase-folded RV plot display an interesting structure. Inspection of the RV residuals in time, however, does not suggest any long-term trend indicative of a tertiary companion, which is consistent with the lack of a detectable tertiary peak in the cross-correlation function. Possible explanations for the residuals are issues with the absolute RV calibration, the RV stability of the reference standards, or the precise placement of the target star in the center of the slit. GP–EBOP attempts to account for this unknown noise component by including an additional jitter term that acts to scale the observational uncertainties. We note that if the origin of this noise component were known, it may be possible to model directly within the fit, but this is beyond the scope of the present analysis.

Figure 7 depicts the system, to scale, at both the primary and secondary eclipse, indicating the geometry responsible for the observed eclipses and RV variations. The model parameters and 1σ uncertainties for AD 3814 are presented in the first results column of Table 6. The light curve and RV modeling with GP–EBOP yields the masses and radii for each star: the primary and secondary masses are $0.3813 \pm 0.0074\ M_{\odot}$ and $0.2022 \pm 0.0045\ M_{\odot}$ with corresponding radii of $0.3610 \pm 0.0033\ R_{\odot}$ and $0.2256\ ^{+0.0063}_{-0.0049}\ R_{\odot}$. The masses of both components are constrained to 2%, and the primary and secondary radii to 1% and 3%, respectively. The fundamental parameters are compatible with the estimated M3.4 $\pm$ 0.1 spectral type and the primary mass estimate from Section 3.1.2. The masses, radii, and effective temperatures (derived in Section 6.1) of AD 3814 are compared to the current suite of stellar evolution models in Section 6.2.

We applied a prior on the system light ratio and priors on the quadratic limb-darkening coefficients (see Table 3). The light ratio was determined from the cross-correlation peak height ratio in a HIRES spectrum taken close to quadrature, which is acceptable as the HIRES spectral range is a reasonable match to the *K2* bandpass. We note that the degeneracy between the surface brightness and radius ratios is not apparent in our posteriors, although it is not expected to be significant in this system given the mass and brightness ratios.

We conclude by noting that this system would benefit from a more detailed modeling of the individual eclipses, incorporating a full starspot model, to assess whether the large-scale underlying starspot distribution can be reconstructed from the eclipses, which track different longitudes on the stellar surfaces over the *K*2 run.

5.2. AD 2615

AD 2615 is an M4.0 high-probability member of Praesepe. The analysis presented here is consistent with the photometric, spectroscopic, and membership information from previous studies. The light curve of AD 2615 that was used in the modeling is shown in Figure 8. One secondary eclipse, at rBJD $\sim$ 2367, was masked following the flare removal process (see Section 4.2). The red line and pink shaded region represent the mean and 2σ uncertainty of the posterior GP–EBOP eclipse model. As with AD 3814, the model is able to capture both the stellar eclipses and the evolving starspot modulation. The model's predictive power can be seen before and after the light curve, where it is able to predict the form of the evolving modulation pattern, given the covariance

[8] rBJD = BJD − 2454833.

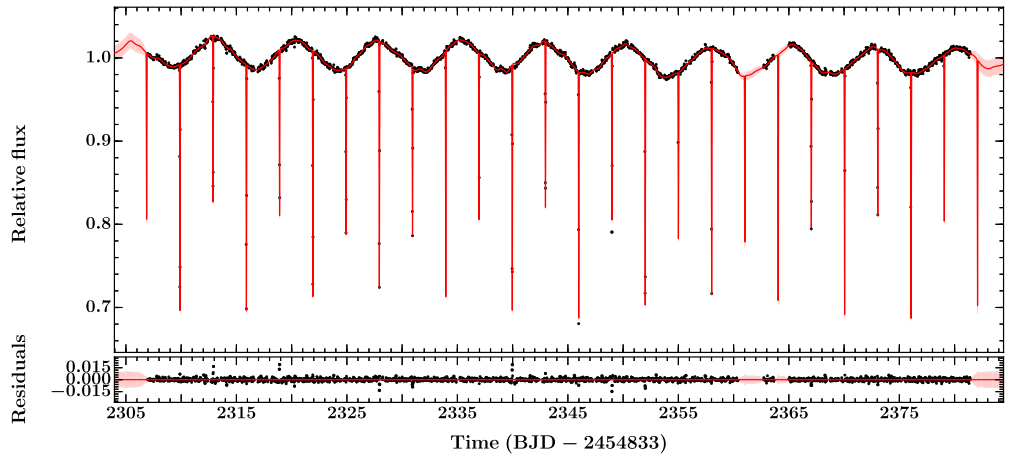

Figure 4. Systematics-corrected *K2* light curve of AD 3814 (black points) with the GP–EBOP model in red. The red line and pink shaded region represent the mean and 2σ uncertainty of the model's predictive posterior distribution, respectively.

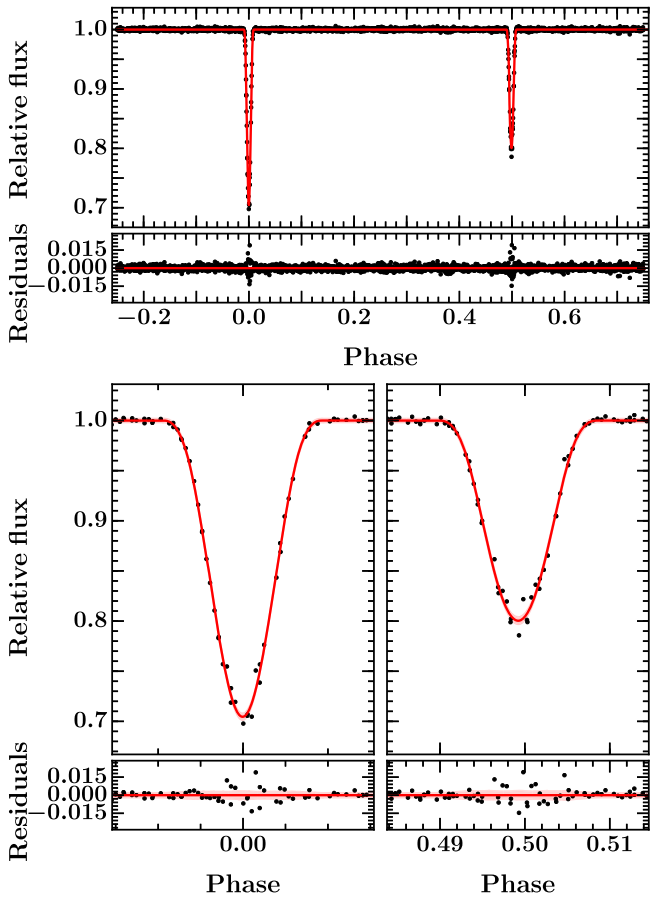

Figure 5. Top panels: phase-folded *K2* light curve of AD 3814 (black), which has been detrended with respect to the Gaussian process model. The red line indicates the median EB model derived from the posterior distribution, i.e., individual draws are calculated across phase space and the median of their paths plotted. Phase zero marks the center of the primary eclipse. Immediately below are the residuals of the fit. Bottom panels: zooms on primary and secondary eclipses (left and right, respectively) with the median model and 2σ uncertainties shown (red line and pink shaded region, respectively). Residuals are shown immediately below.

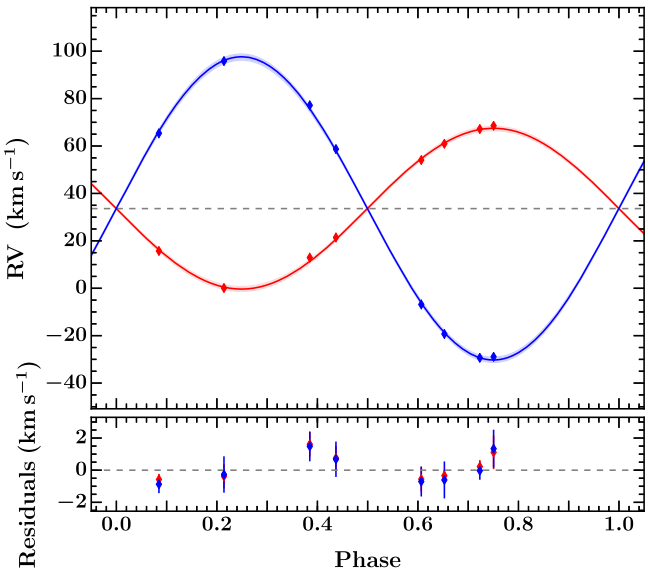

Figure 6. Top: phase-folded RV orbit of AD 3814 with Keck/HIRES RVs for the primary and secondary stars (red and blue, respectively). The lines and shaded regions indicate the median and 2σ uncertainties on the posterior distributions of the RV orbits. The gray horizontal dotted line shows the systemic velocity. Bottom: residuals of the fit.

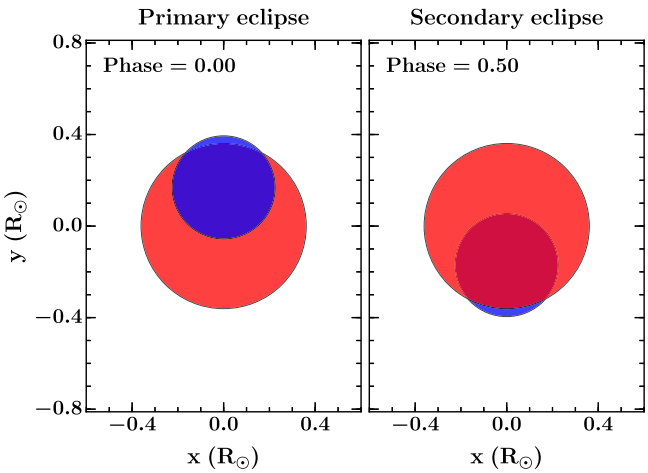

Figure 7. Geometry of AD 3814, to scale, as observed at primary and secondary eclipse. The primary star is shown in red and the secondary in blue.

properties of the data; this also drives the motivated prediction and uncertainty across each eclipse.

Figure 9 shows the phase-folded light curve, which has been detrended with respect to the GP component. The eclipse

Table 3
Spectroscopic Light Ratios and Quadratic Limb-darkening Priors Applied in the GP–EBOP Modeling for ADs 3814, 2615, 3116, and 1508

System	Spectroscopic Light Ratio		Limb-darkening Coefficients and Assumed Model Atmosphere Parameters [a]				
	BJD	l_{sec}/l_{pri}	Component	μ	μ'	T_{eff} (K)	$\log g$ (cgs)
AD 3814	245 7766.9	$0.41^{+0.25}_{-0.19}$	Primary	0.46 ± 0.13	0.21 ± 0.46	3200 ± 200	4.9 ± 0.1
			Secondary	0.49 ± 0.24	0.23 ± 0.76	3100 ± 200	5.0 ± 0.1
AD 2615	245 7766.9	$1.13^{+0.24}_{-0.20}$	Primary & Secondary	0.46 ± 0.13	0.21 ± 0.46	3200 ± 200	4.9 ± 0.1
AD 3116	...	...	Primary	0.46 ± 0.13	0.21 ± 0.46	3200 ± 200	4.9 ± 0.1
			Secondary	0.68 ± 0.17	0.17 ± 0.46	2500 ± 200	5.0 ± 0.1
AD 1508	245 7745.0	$0.63^{+0.41}_{-0.26}$	Primary & Secondary	0.47 ± 0.14	0.20 ± 0.31	3700 ± 200	4.8 ± 0.1

Note.
[a] μ and μ' are the coefficients for the linear and quadratic terms, respectively, of the quadratic limb-darkening law. All limb-darkening coefficients were computed assuming $Z = 0.14 \pm 0.05$.

model is an acceptable fit to the data. There is no clear evidence for increased scatter in the residuals, which suggests that the geometry of the eclipses does not preferentially track bright or dark regions on the stellar surfaces, perhaps because the underlying starspot distribution in AD 2615 is more homogeneous than that in AD 3814.

Figure 10 shows the phase-folded RV orbit (red for primary and blue for secondary). The five HIRES RVs of both stars are well-fit by the Keplerian model. The 2σ uncertainties on the orbits (red and blue shaded regions) increase around quadrature, as expected. The systemic velocity of $V_{sys} = 34.91 \pm 0.39$ km s^{-1} (dashed gray line) is compatible with the cluster's recessional velocity, providing further kinematic evidence of cluster membership. We note that a sixth RV observation was conducted but lay too close to primary eclipse to disentangle the two stellar components and hence was not used in the fit. In principle, we could determine an upper limit on the separation of the two stars and use this as an additional constraint in the modeling. However, at phase = 0.997, the solution is already tightly constrained and hence this upper limit would not place useful constraints on our existing solution. We further note that spectral disentangling may offer an interesting alternative route to RV determination for this system, which could utilize this sixth observation. While traditional spectral disentangling techniques require many high-S/N spectra, powerful new techniques are emerging designed for fewer and lower S/N spectra (e.g., Czekala et al. 2017). It would be interesting to compare the standard CCF-based RV determination with these new spectral disentangling techniques, but this is beyond the scope of the present paper.

Figure 11 depicts the system, to scale, at primary and secondary eclipse, showing the configuration responsible for the observed eclipses. The medians and 1σ uncertainties of the GP–EBOP model posteriors are reported in Table 4 (second results column). The primary and secondary masses are 0.212 ± 0.012 $M_\odot$ and 0.255 ± 0.013 $M_\odot$, with corresponding radii of 0.233 ± 0.013 $R_\odot$ and 0.267 ± 0.014 $R_\odot$. We remind the reader that we define the primary star as the star which, when occulted, gives the deeper eclipse, but that this does not necessarily mean it is the more massive or brighter of the two components, as indeed is the case in this system. The masses and radii are constrained to 6% for the primary and 5% for the secondary. This system would benefit from additional RVs around quadrature to increase the precision of the mass determination. The fundamental parameters are compatible with the estimated M4.0 spectral type but the mass of either component is lower than the estimate from the system's absolute K-band magnitude (Section 3.1.2), presumably because this system is a near-equal-mass binary and so both stars contribute significantly to the K-band flux, resulting in an overestimated single-star mass. The masses, radii, and effective temperatures (see Section 6.1) are compared to stellar evolution models in Section 6.2.

We applied priors on the system light ratio and stellar limb-darkening coefficients (see Table 3). Even though the system is near-equal-mass and brightness, our spectroscopic light ratio was able to break the degeneracy between the surface brightness and radius ratios, which can be a limiting factor in determining radii in such systems.

5.3. AD 3116

AD 3116 is a high-probability M3.9 member of Praesepe. The system sits at the bottom of the cluster sequence (see Figure 1), suggesting that the secondary component contributes little optical light to the total system flux and hence is comparatively low mass.

Analysis of the *K2* light curve and seven HIRES spectra reveals the system to be single lined with eclipses visible only on the primary component, consistent with its position in color–magnitude space. Secondary spectroscopic lines could not be detected, even after dividing the two spectra and looking for similar but weaker patterns in the CCF, which suggests that the secondary contributes very little (<20%–35%) to the system's optical light. Given the lack of a detectable secondary eclipse and secondary RV orbit, the data alone are not able to constrain the solution precisely. There exist two families of solutions: one consisting of a small secondary that fully transits and the other consisting of a larger secondary on a grazing trajectory. The primary RV orbit requires the secondary to be eclipsed, and hence both models find a negligible surface brightness ratio in the *Kepler* band to remain consistent with the lack of a detectable secondary eclipse. For the solution comprising a large ($R_{sec}/R_{pri} \gtrsim 1$), grazing secondary, this would require an unusual object possessing a very low temperature given its radius. Inspection of the system mass function revealed that the secondary lay in the brown dwarf regime ($M_{sec} \sim 55$ M_{Jup}), which further supported the solution comprising a small, fully transiting secondary. We tested the reliability of the primary RV solution to see if individual RVs close to the systemic velocity (i.e., which could be biased by low-level secondary light) may be affecting the eccentricity of the RV orbit and hence the system parameters. We removed all except the three RVs closest to quadrature and, as expected, the model converged again on a solution requiring the secondary

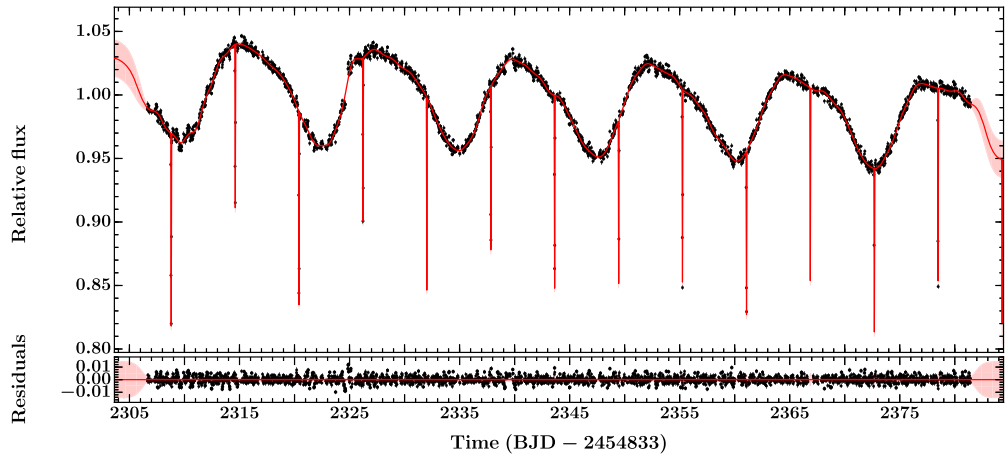

Figure 8. Systematics-corrected *K2* light curve of AD 2615 (black points) with the GP–EBOP model in red. The red line and pink shaded region represent the mean and 2σ uncertainty of the model's predictive posterior distribution.

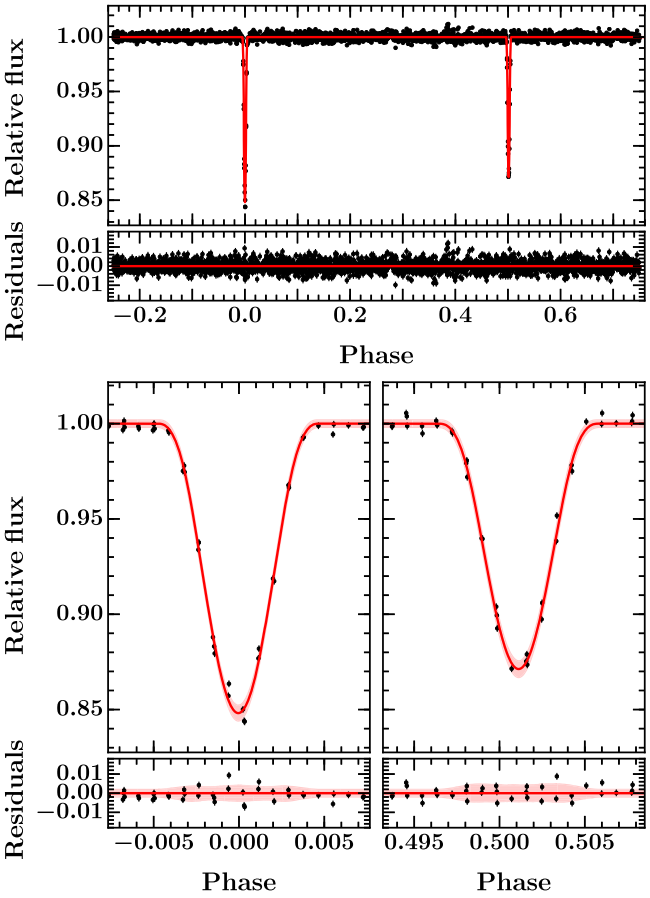

Figure 9. Top panels: phase-folded *K2* light curve of AD 2615 (black), which has been detrended with respect to the Gaussian process model. The red line indicates the median EB model derived from the posterior distribution, i.e., individual draws are calculated across phase space and the median of their paths plotted. Phase zero marks the center of the primary eclipse. Immediately below are the residuals of the fit. Bottom panels: zooms on primary and secondary eclipses (left and right, respectively) with the median model and 2σ uncertainties shown (red line and pink shaded region, respectively). Residuals are shown immediately below.

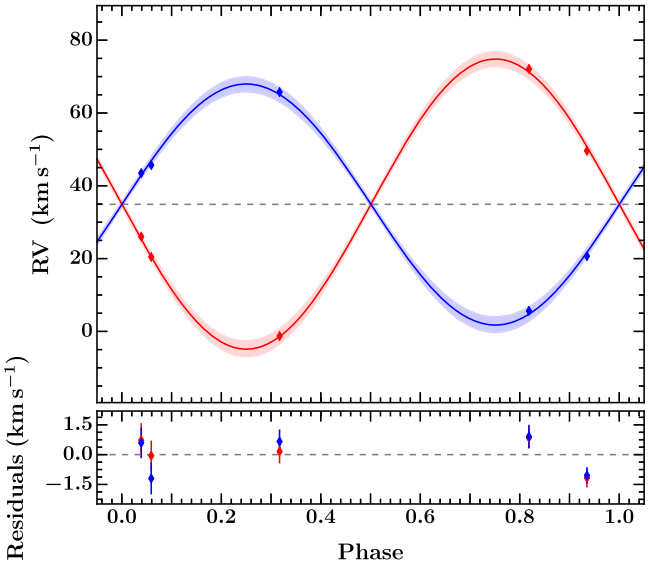

Figure 10. Top: phase-folded RV orbit of AD 2615 with Keck/HIRES RVs for the primary and secondary stars (red and blue, respectively). The lines and shaded regions indicate the median and 2σ uncertainty on the posterior distribution of the RV orbits. The gray horizontal dotted line shows the systemic velocity. Bottom: residuals of the fit.

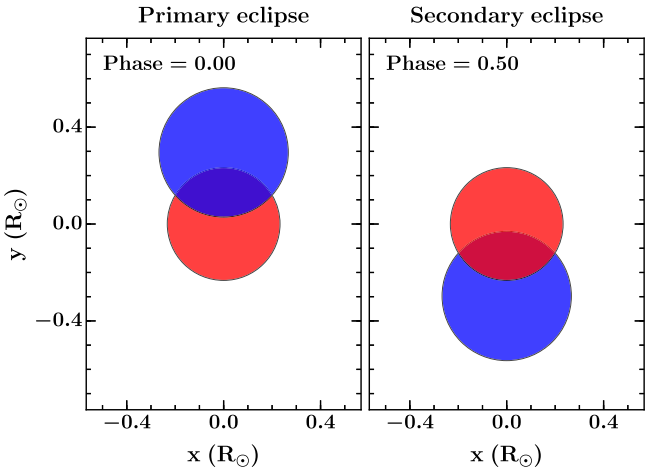

Figure 11. Geometry of AD 2615, to scale, as observed at the primary and secondary eclipse. The primary star is shown in red and the secondary in blue.

to be eclipsed. This, combined with the small primary RV semi-amplitude and lack of secondary spectroscopic lines, rules out a scenario where the secondary is of comparable size and brightness to the primary but there is no secondary eclipse due to the eccentricity of the orbit. All available information

Table 4
Fitted and Derived Parameters of the Models Applied to AD 3814, AD 2615, AD 3116, and AD 1508

Parameter	Symbol	Unit	Value			
			AD 3814	AD 2615	AD 3116	AD 1508
Eclipse Parameters						
Sum of radii	$(R_{\rm pri}+R_{\rm sec})/a$		$0.05044\ ^{+0.00069}_{-0.00055}$	0.02979 ± 0.00034	$0.0845\ ^{+0.0066}_{-0.0053}$	$0.1774\ ^{+0.0066}_{-0.0076}$
Radius ratio	$R_{\rm sec}/R_{\rm pri}$		$0.624\ ^{+0.017}_{-0.010}$	1.15 ± 0.11	$0.3599\ ^{+0.0094}_{-0.0128}$	0.83 ± 0.24
Orbital inclination	i	°	$89.177\ ^{+0.051}_{-0.064}$	88.996 ± 0.013	$88.41\ ^{+0.49}_{-0.42}$	$80.54\ ^{+0.46}_{-0.39}$
Orbital period	P	days	6.015717 ± 0.000013	11.615254 ± 0.000073	1.9827960 ± 0.0000064	$1.5568370\ ^{+0.0000100}_{-0.0000090}$
Time of eclipse center	$T_{\rm prim}$	BJD	$2457178.982842 \pm 0.000059$	$2457176.63998 \pm 0.00019$	$2457178.817792 \pm 0.000080$	$2457147.26784 \pm 0.00026$
	$\sqrt{e}\cos\omega$		$-0.0301\ ^{+0.0103}_{-0.0057}$	$0.0337\ ^{+0.0067}_{-0.0128}$	$0.364\ ^{+0.016}_{-0.026}$	$-0.0081\ ^{+0.0069}_{-0.0094}$
	$\sqrt{e}\sin\omega$		0.031 ± 0.034	0.020 ± 0.052	0.04 ± 0.14	$0.010\ ^{+0.049}_{-0.041}$
Central surface brightness ratio	J_{K2}		0.748 ± 0.034	0.950 ± 0.060	$0.0051\ ^{+0.0049}_{-0.0036}$	$0.90\ ^{+0.30}_{-0.21}$
Primary linear LDC [a]	$u_{\rm pri\ K2}$		0.54 ± 0.20	0.51 ± 0.13	0.66 ± 0.16	0.48 ± 0.14
Primary nonlinear LDC[a]	$u'_{\rm pri\ K2}$		0.24 ± 0.29	0.31 ± 0.22	0.03 ± 0.23	0.22 ± 0.24
Secondary linear LDC[a]	$u_{\rm sec\ K2}$		0.39 ± 0.11	0.41 ± 0.13	0.43 ± 0.13	0.44 ± 0.14
Secondary nonlinear LDC[a]	$u'_{\rm sec\ K2}$		0.12 ± 0.21	$0.04\ ^{+0.25}_{-0.18}$	0.12 ± 0.26	0.12 ± 0.23
Out-of-eclipse Variability Parameters						
Amplitude	A_{K2}	%	$0.00785\ ^{+0.00077}_{-0.00057}$	0.0179 ± 0.0023	$0.0103\ ^{+0.0033}_{-0.0020}$	$0.136\ ^{+0.085}_{-0.136}$
Timescale of SqExp term	$l_{\rm SE\ K2}$	days	$8.55\ ^{+0.43}_{-0.36}$	16.97 ± 0.97	$7.32\ ^{+0.90}_{-0.67}$	…
Scale factor of ExpSine2 term	$\Gamma_{\rm ESS\ K2}$	days	11.5 ± 4.0	$9.56\ ^{+0.96}_{-0.82}$	$0.55\ ^{+0.27}_{-0.20}$	…
Period of ExpSine2 term	$P_{\rm ESS\ K2}$	days	$7.375\ ^{+0.059}_{-0.069}$	$12.150\ ^{+0.074}_{-0.062}$	2.252 ± 0.020	…
Timescale of Matern32 term	$l_{\rm M32\ K2}$	days	…	…	…	223.6 ± 2.3
White noise scale factor	σ_{K2}		1.901 ± 0.039	1.448 ± 0.02	1.363 ± 0.019	$1.329\ ^{+0.031}_{-0.023}$
RV Parameters						
Systemic velocity	$V_{\rm sys}$	km s^{-1}	33.60 ± 0.24	34.91 ± 0.39	$34.93\ ^{+0.61}_{-0.53}$	33.1 ± 1.7
Primary RV semi-amplitude	$K_{\rm pri}$	km s^{-1}	33.90 ± 0.39	$39.86\ ^{+0.80}_{-0.88}$	$18.66\ ^{+0.95}_{-1.00}$	98 ± 15
Secondary RV semi-amplitude	$K_{\rm sec}$	km s^{-1}	63.93 ± 0.49	$33.12\ ^{+0.83}_{-0.89}$	…	84 ± 14
HIRES jitter term	$\sigma_{\rm HIRES}$	km s^{-1}	$0.50\ ^{+0.37}_{-0.30}$	$0.95\ ^{+0.48}_{-0.35}$	$0.93\ ^{+1.18}_{-0.62}$	$1.6\ ^{+2.5}_{-1.2}$
Fundamental Parameters						
Primary mass	$M_{\rm pri}$	$M_\odot$	0.3813 ± 0.0074	0.212 ± 0.012	0.276 ± 0.020 [b]	$0.45\ ^{+0.19}_{-0.14}$
Secondary mass	$M_{\rm sec}$	$M_\odot$	0.2022 ± 0.0045	0.255 ± 0.013	0.0517 ± 0.0041 (54.2 ± 4.3)[c,d]	$0.53\ ^{+0.22}_{-0.16}$
Primary radius	$R_{\rm pri}$	$R_\odot$	0.3610 ± 0.0033	0.233 ± 0.013	0.29 ± 0.08 [e]	$0.549\ ^{+0.099}_{-0.082}$
Secondary radius	$R_{\rm sec}$	$R_\odot$	$0.2256\ ^{+0.0063}_{-0.0049}$	0.267 ± 0.014	0.10 ± 0.03 (1.02 ± 0.28)[d,f]	$0.454\ ^{+0.094}_{-0.101}$
Primary effective temperature	$T_{\rm pri}$	K	$3211\ ^{+54}_{-36}$	$3152\ ^{+57}_{-40}$	3184 ± 29	$3767\ ^{+99}_{-85}$
Secondary effective temperature	$T_{\rm sec}$	K	$3103\ ^{+53}_{-39}$	$3131\ ^{+56}_{-38}$	1639 ± 248	$3693\ ^{+122}_{-135}$
Mass sum	$M_{\rm pri}+M_{\rm sec}$	$M_\odot$	0.583 ± 0.011	0.468 ± 0.023	…	$0.98\ ^{+0.38}_{-0.29}$
Radius sum	$R_{\rm pri}+R_{\rm sec}$	$R_\odot$	$0.5868\ ^{+0.0084}_{-0.0073}$	$0.4991\ ^{+0.0096}_{-0.0102}$	…	1.00 ± 0.13
Semimajor axis	a	$R_\odot$	11.630 ± 0.073	16.75 ± 0.28	…	5.67 ± 0.65
Eccentricity	e		$0.00194\ ^{+0.00253}_{-0.00057}$	$0.00254\ ^{+0.00406}_{-0.00078}$	$0.146\ ^{+0.024}_{-0.016}$	$0.00108\ ^{+0.00347}_{-0.00078}$
Longitude of periastron	ω	°	$116\ ^{+39}_{-256}$	$27\ ^{+44}_{-69}$	5 ± 20	$91\ ^{+29}_{-207}$

Table 4
(Continued)

Parameter	Symbol	Unit	Value			
			AD 3814	AD 2615	AD 3116	AD 1508
Primary surface gravity	$\log g_{\rm pri}$	(cm s^{-2})	$4.9040^{+0.0073}_{-0.0064}$	5.031 ± 0.048	⋯	4.61 ± 0.13
Secondary surface gravity	$\log g_{\rm sec}$	(cm s^{-2})	$5.037^{+0.019}_{-0.026}$	$4.993^{+0.042}_{-0.035}$	⋯	4.84 ± 0.20
Primary synchronized velocity	$V_{\rm pri\ sync}$	km s^{-1}	3.036 ± 0.028	1.014 ± 0.058	⋯	17.8 ± 3.2
Secondary synchronized velocity	$V_{\rm sec\ sync}$	km s^{-1}	$1.898^{+0.053}_{-0.041}$	$1.162^{+0.050}_{-0.059}$	⋯	14.7 ± 3.3
Synchronization timescale	$t_{\rm sync}$	Myr	27.29 ± 0.49	152.6 ± 4.7	⋯	$0.0510^{+0.0120}_{-0.0090}$
Circularization timescale	$t_{\rm circ}$	Gyr	17.30 ± 0.10	467.6 ± 1.5	⋯	$0.01040^{+0.00033}_{-0.00013}$

Notes.
[a] LDC = limb-darkening coefficient.
[b] Derived from the empirical relations of Benedict et al. (2016).
[c] Derived from the system mass function.
[d] Units in brackets are relative to Jupiter.
[e] Derived from the empirical relations of Mann et al. (2015).
[f] Derived from the light curve radius ratio and the empirically determined primary radius.

and tests pointed toward a very low-mass, small, and cool secondary component.

We therefore chose to place loose uniform priors on the radius ratio and surface brightness ratio to encourage the solution toward a physically sensible secondary component. These priors were $0.0 \leqslant R_{\rm sec}/R_{\rm pri} \leqslant 0.46$ and $0.0 \leqslant J_{K2} \leqslant 0.25$, which, given the expected primary star properties (see Section 3.1.2) and secondary star mass estimate, act simply to exclude physically implausible solutions and do not act to constrain the remaining physically plausible solutions. We performed further tests allowing $R_{\rm sec}/R_{\rm pri}$ and J_{K2} to extend up to 0.75 and 0.35, respectively, but find consistent posterior values.

The model fit is shown in Figures 12–15, whose descriptions are the same as for ADs 3814 and 2615 in Sections 5.1 and 5.2 above. The model is a good fit to the primary eclipse and large-scale evolving starspot structure in the *K2* light curve (Figure 6). We note that two primary eclipses, at rBJD $\sim$ 2319 and 2350, were masked following the flare removal process (see Section 4.2). Figure 13 shows the phase-folded and GP-detrended light curve: the primary eclipse is well-fit, although there is a modest increase in the residual scatter, which is larger than in AD 2615 but smaller than in AD 3814. The RV data suggest a moderately eccentric orbit ($e \sim 0.15$; see Figure 14) with a systemic velocity of $V_{\rm sys} = 34.93\ ^{+0.61}_{-0.53}$ km s^{-1} (dashed gray line). This is consistent with the cluster's recessional velocity, providing additional kinematic evidence of cluster membership.

Using the empirical relations of Benedict et al. (2016) and assuming the van Leeuwen (2009) cluster distance of 181.5 ± 6.0 pc, the $K_{\rm s}$ magnitude of AD 3116 implies a primary mass of $M_{\rm pri} = 0.28 \pm 0.02\ M_{\odot}$, where the uncertainty arises equally from the empirical relation scatter and our assumed 0.1 mag uncertainty on the quoted $K_{\rm s}$ value. We checked this value using the empirical relations of Mann et al. (2015) and find $M_{\rm pri} \sim 0.29\ M_{\odot}$, consistent with the Benedict et al. value. Taking the Benedict value, the mass function from our final solution then yields $M_{\rm sec} = 54.2 \pm 4.3\ M_{\rm Jup}$. This is one of only $\sim$20 known transiting brown dwarfs (e.g., Csizmadia 2016; Nowak et al. 2017; Bayliss et al. 2017) and the primary component is one of only three M-dwarfs known to host a transiting brown dwarf. Furthermore, this is only the second known transiting brown dwarf in an open cluster (i.e., where the age is well-constrained), and the first younger than a Gyr.

Figure 15 shows the system geometry at primary and secondary eclipse. That the brown dwarf is fully occulted yet shows no detected signature in the *K2* band theoretically allows us to place an upper limit on the optical reflected light and hence the albedo of the object. Using the Mann et al. (2015) empirical relations to estimate the primary radius, and hence the secondary radius and semimajor axis from our light curve modeling, we can estimate the system scale. This then allows us to compute the angle on the sky that the brown dwarf subtends as seen from the primary. With $R_{\rm sec} \sim 0.11\ R_{\odot}$ and $a \sim 4.7\ R_{\odot}$, the brown dwarf intercepts $\sim$0.007% of the visible light from the primary star. Therefore, even if the brown dwarf reflected all incident flux (i.e., an albedo of 1), we would not detect a drop in flux in the *K2* light curve when the brown dwarf is occulted.

We applied priors on the limb-darkening coefficients (see Table 3). The secondary temperature was set to be as low as the PHOENIX models allow but is likely still too high (see Table 5). However, as the secondary gives no detectable eclipse, it makes no significant difference to the presented solution. Given that the system is single lined, we did not place a prior on the system light ratio in the *K2* band.

5.4. AD 1508

AD 1508 is a high-probability M0.1 member of Praesepe, which sits high above the cluster sequence (see Figure 1), suggesting a near-equal-mass system. The preliminary analysis presented here is consistent with this picture. The *K2* light curve of AD 1508 (see Figures 2 and 3; bottom panels) is dominated by evolving starspot modulation at the few percent level. Very shallow grazing eclipses are also present with a depth of less than 1%. We obtained only three RVs for this system, which unfortunately fell close to primary and secondary eclipses (see Table 2). Given this, and the shallow eclipses, a precise solution is not possible. Instead, we provide our initial analysis and offer the system to the community for further pursuit.

The *K2* light curve and three Keck/HIRES RVs were simultaneously modeled with GP–EBOP. However, given the preliminary nature of the modeling, and unlike the other three systems, we opted to simplify the light curve analysis by performing an initial detrending of the starspot modulation and then modeled the residuals with GP–EBOP to analyze the stellar eclipses. To do this, the OOE light curve was flattened through two iterations of a cubic basis spline with knots every 2 hr and rejection of 0.5σ outliers. Figure 16 shows the resulting detrended light curve that was modeled with GP–EBOP. Low-level (likely systematic) residual variations are present, which show a relatively rough behavior. Accordingly, we chose a Matern 3/2 kernel for the GP component, which is given by

$$k_{\rm M32}(t_i, t_j) = A^2\left(1 + \frac{\sqrt{3}\,|t_i - t_j|}{l}\right)\exp\left(-\frac{\sqrt{3}\,|t_i - t_j|}{l}\right), \quad (5)$$

where A is the amplitude and l is the characteristic timescale of the variations.

Detrending with respect to the GP component and phase-folding on the orbital period, as shown in Figure 17, we see that the eclipses are well-fit by the model. There is no significant evidence of increased scatter across the eclipses. We note that the light curve of AD 1508 appears noisy in comparison to the other systems discussed here, even though it is significantly brighter. This is simply because the plot scales in Figures 16 and 17 are small as the eclipses are shallow and the starspot modulation has already been detrended. It is not a reflection of the true noise level in this system: the point-to-point scatter of all systems discussed here decreases with system brightness, as expected.

The phase-folded RV orbit is shown in Figure 18, which, given only three RVs at non-optimal phases, is not well-constrained. This is reflected in the large 2σ uncertainties on the posterior orbits (red and blue for the primary and secondary stars, respectively). Nonetheless, the systemic velocity is relatively well-constrained at $V_{\rm sys} = 33.1 \pm 1.7$ km s^{-1}, which is consistent with the cluster recessional velocity and hence provides further kinematic evidence of Praesepe membership. Figure 19 shows the system, to scale, at primary and secondary eclipse. The shallow eclipses simply result from the very grazing trajectory of the stellar orbits, as viewed from Earth.

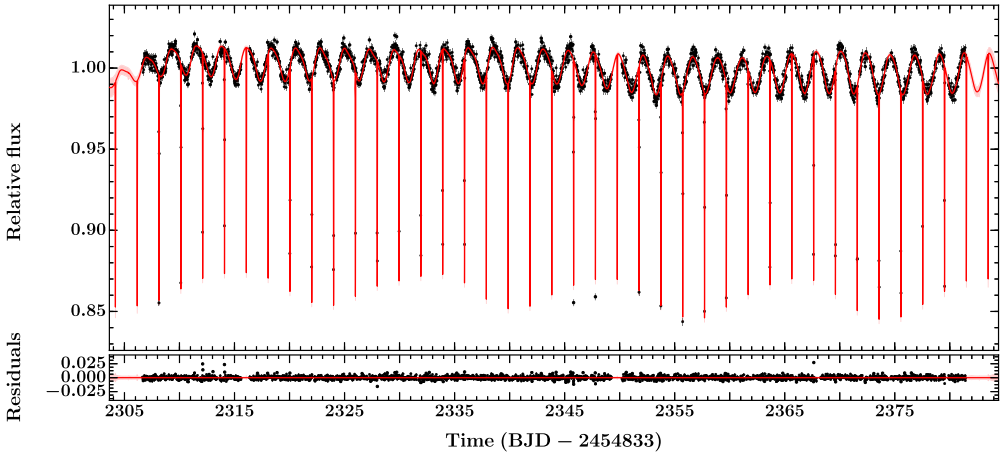

Figure 12. Systematics-corrected *K2* light curve of AD 3116 (black points) with the GP–EBOP model in red. The red line and pink shaded region represent the mean and 2σ uncertainty of the model's predictive posterior distribution.

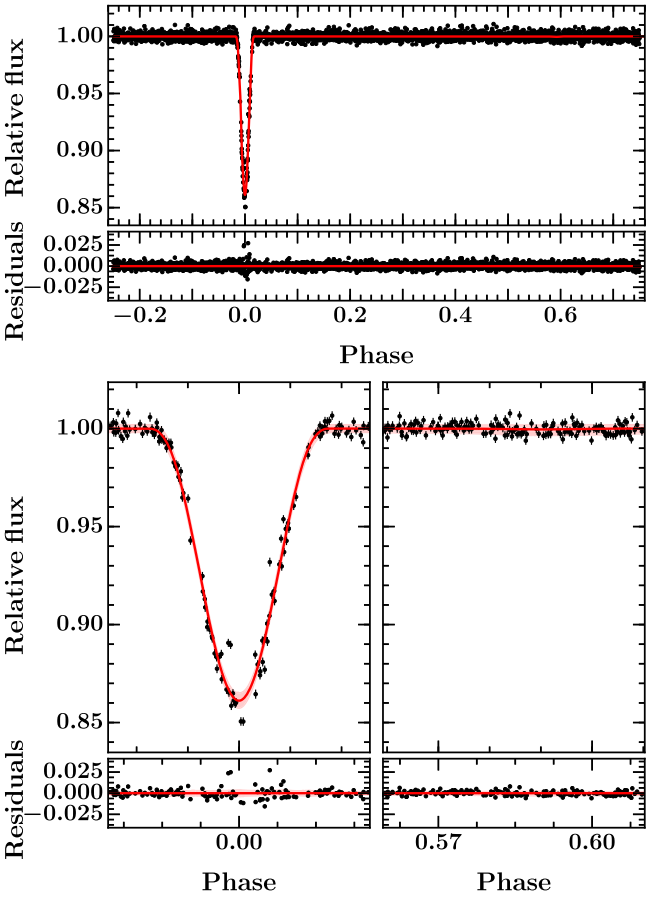

Figure 13. Top panels: phase-folded *K2* light curve of AD 3116 (black), which has been detrended with respect to the Gaussian process model. The red line indicates the median EB model derived from the posterior distribution, i.e., individual draws are calculated across phase space and the median of their paths plotted. Phase zero marks the center of the primary eclipse. Immediately below are the residuals of the fit. Bottom panels: zooms on primary and secondary eclipses (left and right, respectively) with the median model and 2σ uncertainties shown (red line and pink shaded region, respectively). Residuals are shown immediately below.

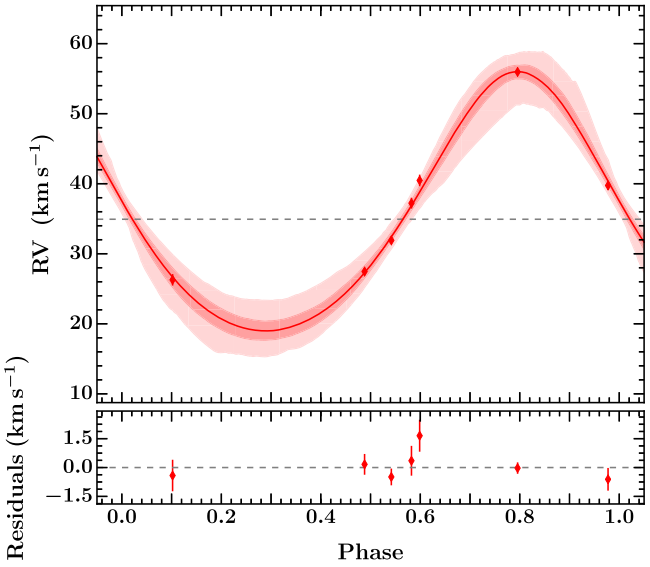

Figure 14. Top: phase-folded RV orbit of AD 3116 with Keck/HIRES RVs for the primary and secondary stars (red and blue, respectively). The line and shaded regions indicate the median and 1σ and 2σ uncertainties on the posterior distribution of the primary RV orbit. The gray horizontal dotted line shows the systemic velocity. Bottom: residuals of the fit.

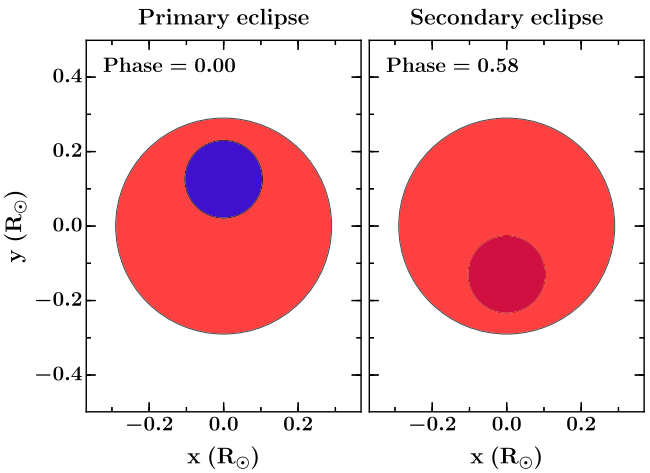

Figure 15. Geometry of AD 3116, to scale, as observed at primary and secondary eclipse. The primary star is shown in red and the secondary in blue.

The median and 1σ uncertainties resulting from our preliminary analysis are reported in Table 4 (fourth results column). Given the available data, significant uncertainties exist in the derived masses and radii. The primary and

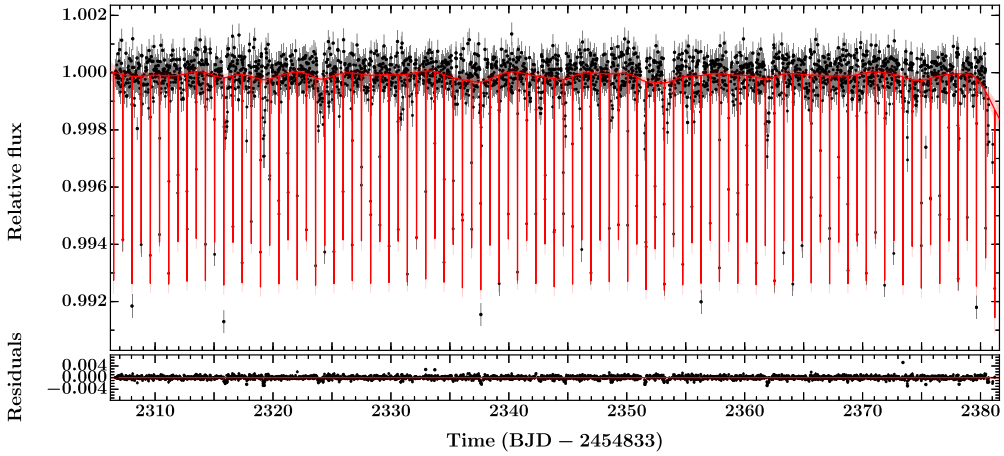

Figure 16. Systematics-corrected *K2* light curve of AD 1508 (black points) with the GP–EBOP model in red. The red line and pink shaded region represent the mean and 2σ uncertainty of the model's predictive posterior distribution.

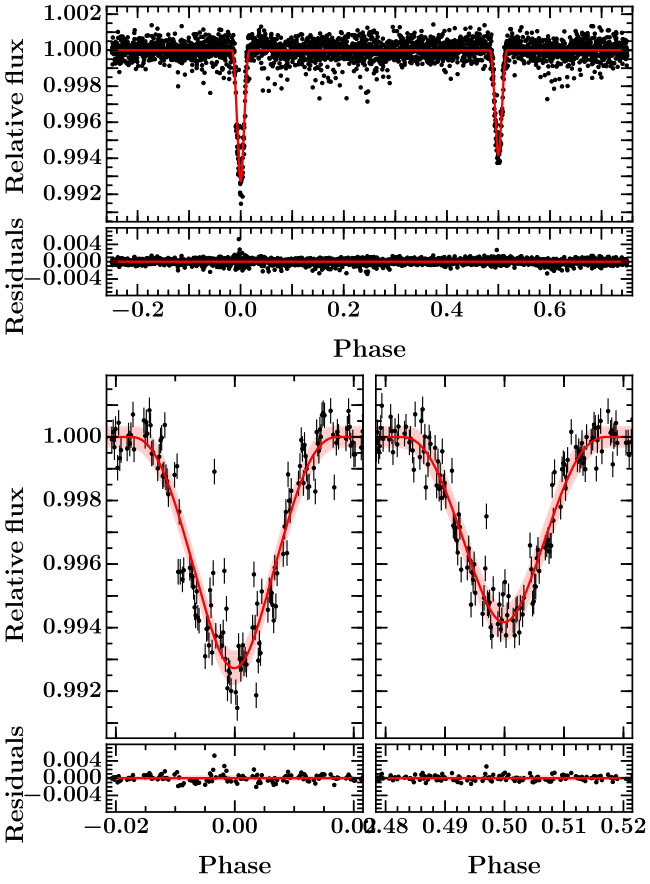

Figure 17. Top panels: phase-folded *K2* light curve of AD 1508 (black), which has been detrended with respect to the Gaussian process model. The red line indicates the median EB model derived from the posterior distribution, i.e., individual draws are calculated across phase space and the median of their paths plotted. Phase zero marks the center of the primary eclipse. Immediately below are the residuals of the fit. Bottom panels: zooms on the primary and secondary eclipses (left and right respectively) with the median model and 2σ uncertainties shown (red line and pink shaded region, respectively). Residuals are shown immediately below.

secondary masses are $0.45\ ^{+0.19}_{-0.14}\ M_\odot$ and $0.53\ ^{+0.22}_{-0.16}\ M_\odot$ with corresponding radii of $0.549\ ^{+0.099}_{-0.082}\ R_\odot$ and $0.454\ ^{+0.094}_{-0.101}\ R_\odot$. The solution is currently limited by the lack of RV constraints and future analysis would benefit from additional RV measurements, especially around quadrature. Nonetheless, the

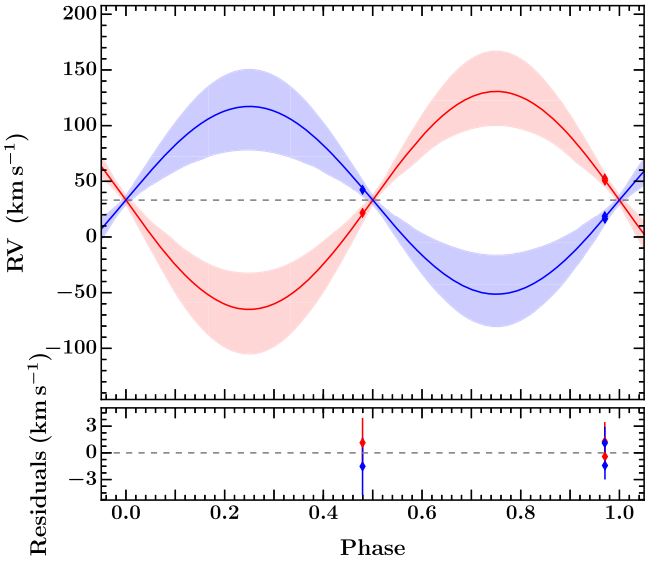

Figure 18. Top: phase-folded RV orbit of AD 1508 with Keck/HIRES RVs for the primary and secondary stars (red and blue, respectively). The lines and shaded regions indicate the median and 2σ uncertainty on the posterior distribution of the RV orbits. The gray horizontal dotted line shows the systemic velocity. Bottom: residuals of the fit.

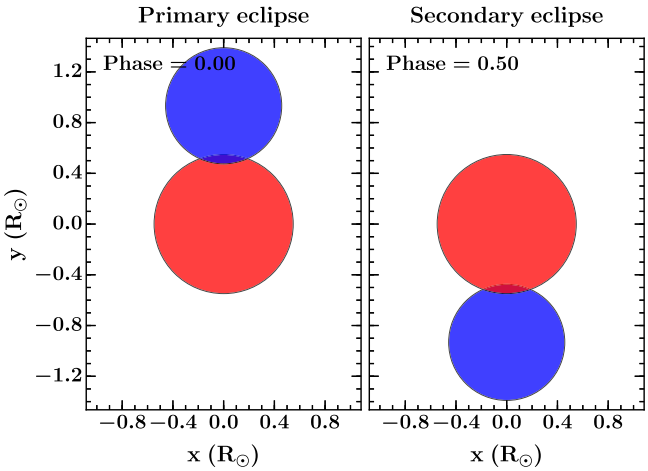

Figure 19. Geometry of AD 1508, to scale, as observed at primary and secondary eclipse. The primary star is shown in red and the secondary in blue.

fundamental parameters are compatible with the estimated M0.1 ± 0.1 spectral type and the primary mass estimate from Section 3.1.2. Given the existing uncertainties, we do not compare this system to stellar evolution models in Section 6.2.

We applied priors on the system light ratio and limb-darkening coefficients (see Table 3). Although large uncertainties remain, the spectroscopic light ratio was able to break the degeneracy between the surface brightness and radius ratios, which can be a limiting factor in determining individual radii in near-equal-mass and brightness systems.

6. Discussion

The direct determination of fundamental stellar parameters offers an opportunity to test stellar evolution models. The fundamental predictions of these models are the radius and $T_{\rm eff}$ for a star of given mass and metallicity as a function of age. Ideally, therefore, we would be able to determine the mass, radius, and $T_{\rm eff}$ of both stars as, together, these offer a particularly strong test of stellar evolution theory. However, while the masses and radii of stars in EBs naturally fall out of the joint light curve and RV modeling, estimating effective temperatures is more challenging. In Section 6.1, we present a method of simultaneously estimating the effective temperature of both stars and the distance to the system in a manner that makes full and correct use of the light and RV constraints. We then compare our $T_{\rm eff}$ and distances to empirical $T_{\rm eff}$ relations and to previous distance estimates to Praesepe. In Section 6.2, we compare our masses, radii, and $T_{\rm eff}$ to the predictions of stellar evolution models for individual systems and also place the newly characterized EBs in the context of other known low-mass EBs and briefly discuss the constraints that can be placed on the age of Praesepe. Through this model comparison and in Section 6.3, where we comment on the synchronization of the new EBs, we discuss several astrophysical implications of our findings.

6.1. Simultaneous Determination of Effective Temperatures and Distance from the SED

The standard method for estimating $T_{\rm eff}$ is the following: (1) either estimate the primary star $T_{\rm eff}$ from system colors adopting empirical single-star relations, or use (typically) low-resolution spectra to infer a combined spectral type (SpT) and convert this into a primary star $T_{\rm eff}$. (2) Estimate the secondary star $T_{\rm eff}$ from the primary $T_{\rm eff}$ using the light curve surface brightness (and hence temperature) ratio. There are a number of issues with this approach: empirical color–$T_{\rm eff}$ and SpT–$T_{\rm eff}$ relations for single stars are not necessarily applicable to all binary systems and the temperature ratio estimated from the light curve is specific to that band, i.e., $(T_{\rm sec}/T_{\rm pri})_{\rm band}$; it is not a $T_{\rm eff}$ ratio.

A more direct approach would be to model the system's spectra, but to do so would require high-S/N data, which would normally require the co-adding of spectra. Although feasible for single-star systems, this is not possible for binaries as there are two varying components. One approach would be to disentangle the spectra into their individual components and model these directly to estimate the $T_{\rm eff}$ of each star (e.g., Czekala et al. 2015, 2017). However, while powerful, this approach is both time and computationally intensive, and the distance to the system remains unknown (unless the spectra are also flux calibrated).

A method for simultaneously determining the $T_{\rm eff}$ of both stars, and the distance to the system, is to model the system's spectral energy distribution (SED). This approach is not computationally intensive, does not rely on empirical single-star relations, and readily incorporates priors from the joint light curve and RV modeling. Importantly, with respect to the last point, it correctly interprets the band-specific surface brightness ratio from the light curve modeling. Therefore, we simultaneously estimate the $T_{\rm eff}$ of both the stars and distance to ADs 3814, 2615, 3116, and 1508 using the following method.

1. SEDs were constructed using broadband magnitudes readily available in the literature. We obtained SDSS *ugriz* magnitudes from the Sloan Digital Sky Survey Data Release 13, and 2MASS JHK$_{\rm s}$ and *WISE* data from the NASA/IPAC Infrared Science Archive. These are reported in Table 1 along with their formal measurement uncertainties.
2. Model grids of both BT-SETTL (Allard et al. 2012) and PHOENIX v2 model spectra (Husser et al. 2013) were convolved with commonly available bandpasses (*ugriz*, *UBVRI*, 2MASS JHK$_s$, *Spitzer*/IRAC, *WISE*, and *Kepler*) to create a model grid of bandpass fluxes.
3. Each SED was modeled by interpolating the model grids in $T_{\rm eff}$–$\log g$ space. We opted to fix the metallicity at $Z = 0.0$ given the cluster [Fe/H] value, but note that it is possible to include in the interpolation.
4. The parameters of the fit were: the $T_{\rm eff}$, radius, and $\log g$ of each star; the distance to the system; the interstellar extinction; and the uncertainty scale factor ($T_{\rm pri}$, $T_{\rm sec}$, $R_{\rm pri}$, $R_{\rm sec}$, $\log g_{\rm pri}$, $\log g_{\rm sec}$, $d_{\rm sys}$, $A_{\rm v}$, and σ_s). The radii and $\log g$ have priors from the joint light curve and RV solution, $A_{\rm v}$ had a prior determined for the cluster (Taylor 2006), and the temperatures, distance, and uncertainty scale factors had uninformative priors. The uncertainties on the magnitudes were initially set by adding the observed variability level to the formal measurement errors in quadrature and a further inflation term (σ_s) was then fit for.
5. The posterior parameter space was explored using `emcee` with 50,000 steps and 196 "walkers." Convergence was assessed using the Gelman–Rubin diagnostic plus examination of individual sections of the chains. A conservative burn-in comprising the first 25,000 steps for all systems was estimated, and parameter distributions were derived from the remainder after thinning each chain based on the autocorrelation lengths of each parameter.
6. This method also gives the option of placing additional priors in the modeling. For example, one can place a prior, from the light curve modeling, on the surface brightness ratio between the two stars–in the band observed–rather than incorrectly placing a $T_{\rm eff}$ ratio constraint. In the case of single-lined systems, radius ratio constraints and surface brightness upper limits can also be placed.

Both BT-SETTL and PHOENIX v2 model spectra are able to reproduce the broadband magnitudes of ADs 3814, 2615, 3116, and 1508. We note, however, that the BT-SETTL models consistently underpredict the optical *r*-band fluxes, whereas the PHOENIX v2 models predict higher red-optical fluxes in agreement with the data for all sources. Accordingly, in

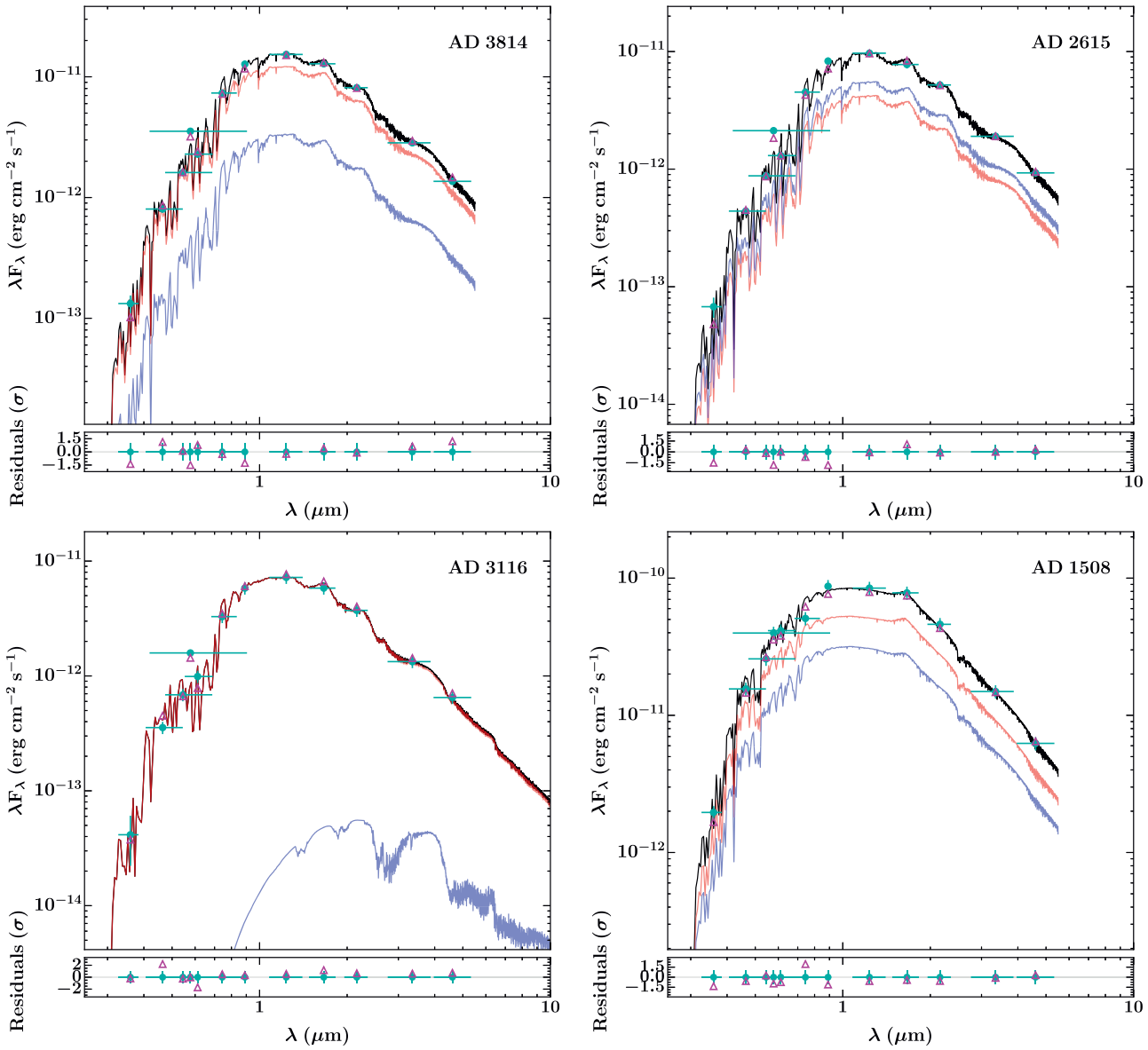

Figure 20. Spectral energy distributions (SEDs) of the four new EBs. Clockwise from top left: ADs 3814, 2615, 1508, and 3116. Cyan points represent the observed SED, which has been constructed from the broadband magnitudes reported in Table 1 (horizontal error bars indicate each band's spectral coverage). The primary and secondary star spectra are shown in red and blue, respectively. Their combined spectrum is shown in black and the hollow magenta triangles show the combined model convolved with the *ugriz*, *V*, K_p, *JHK*, and *WISE* 1 & 2 bands. The models shown for ADs 3814, 2615, and 1508 are the PHOENIX v2 models as these produce a better fit to the data than the BT-SETTL models. However, we show the BT-SETTL models for AD 3116 as the PHOENIX models do not extend to low enough temperatures to explain the secondary component.

Figure 20 we show the PHOENIX v2 model fits to the observed broadband magnitudes of ADs 3814, 2615, and 1508 reported in Table 1 (for AD 3116, we show the BT-SETTL fit as the PHOENIX models do not extend to low enough temperatures to explain the secondary brown dwarf component). The $T_{\rm eff}$ and distance values derived from our SED-fitting procedure with both the BT-SETTL and PHOENIX v2 models are reported in Table 5 along with the empirical relation predictions of Mann et al. (2015) and David et al. (2016b). We discuss the effective temperature and distance estimates in the following two sections.

6.1.1. Effective Temperatures

We find that the BT-SETTL model temperatures are typically ∼40 K hotter than the PHOENIX v2 values, although both sets of temperatures agree to within 1σ. They are also both in agreement with the temperatures predicted by empirical relations. We note that both sets of empirical relations used the BT-SETTL models to calibrate their temperature scale, and hence caution should be applied when interpreting the slightly closer agreement between the empirical relations and BT-SETTL SED temperatures than with the PHOENIX v2 values.

Given the slight offset between the BT-SETTL and PHOENIX temperatures, we opted to combine the two predictions for each star as our final $T_{\rm eff}$ values. These are reported in Table 5 as the "combined" model and are $T_{\rm pri} = 3211\ ^{+54}_{-36}$ K and $T_{\rm sec} = 3103\ ^{+53}_{-39}$ K for AD 3814, $T_{\rm pri} = 3152\ ^{+57}_{-40}$ K and $T_{\rm sec} = 3131\ ^{+56}_{-38}$ K for AD 2615, and $T_{\rm pri} = 3767\ ^{+99}_{-85}$ K and $T_{\rm sec} = 3693\ ^{+122}_{-135}$ K for AD 1508. For AD 3116, we used only the BT-SETTL models given the expected temperature of the brown dwarf secondary.

Table 5
Effective Temperatures and Distance Values for Each EB Estimated from SED Modeling and the Empirical Relations of Mann et al. (2015) and David et al. (2016b)

Method[a]	Model[b]	$T_{\rm eff}$[c]		Distance
		Primary (K)	Secondary (K)	(pc)
		AD 3814		
SED	PHOENIX	3193 ± 17	3085 ± 21	$168.8^{+6.1}_{-7.3}$
SED	BT-SETTL	3230 ± 36	3121 ± 35	172.1 ± 9.3
ER	M15	3241 ± 76	3013 ± 79	172 ± 12
ER	D16	3251	3023	⋯
SED	Combined	3211^{+54}_{-36}	3103^{+53}_{-39}	$170.4^{+11.0}_{-8.9}$
		AD 2615		
SED	PHOENIX	3132 ± 21	3112 ± 20	177.2 ± 7.9
SED	BT-SETTL	3172 ± 37	3150 ± 37	181 ± 11
ER	M15	3187 ± 75	3145 ± 90	177 ± 15
ER	D16	3197	3156	⋯
SED	Combined	3152^{+57}_{-40}	3131^{+56}_{-38}	179^{+13}_{-10}
		AD 3116		
SED	BT-SETTL	3184 ± 29	1639 ± 248	⋯
ER	M15	3237 ± 74	880 ± 217	183 ± 14
ER	D16	3236	880	⋯
		AD 1508		
SED	PHOENIX	3754 ± 78	3679 ± 121	164 ± 22
SED	BT-SETTL	3779 ± 87	3706 ± 117	167 ± 23
ER	M15	3738 ± 76	3639 ± 284	156 ± 28
ER	D16	3746	3649	⋯
SED	Combined	3767^{+99}_{-85}	3693^{+122}_{-135}	166^{+25}_{-23}

Notes.
[a] SED = spectral energy distribution and ER = empirical relations.
[b] M15 = empirical relations from Mann et al. (2015); D16 = David et al. (2016b) polynomial fit to the color and temperature data presented in Pecaut & Mamajek (2013).
[c] For the two sets of empirical relations, the secondary $T_{\rm eff}$ is estimated using the GP–EBOP temperature ratio in the *K2* band as a proxy for the $T_{\rm eff}$ ratio.

While both SED modeling and empirical relations yield consistent results, the SED modeling constraints are significantly tighter (even combining both sets of results), which is perhaps unsurprising given that they are system specific and capitalize on the joint light curve and RV modeling constraints. Furthermore, interpreting the temperature ratio from the light curve modeling as a genuine $T_{\rm eff}$ ratio is incorrect in all cases where the bandpass observed does not cover the majority of the integrated spectra of both EB components, and the system is not equal mass. For both ADs 3814 and 2615, using the *Kepler* bandpass temperature ratio as a $T_{\rm eff}$ ratio (as required when using empirical relations) results in a steeper temperature scale than the light curve modeling results actually imply, i.e., the secondary is predicted to be cooler than expected relative to the primary temperature. This effect is most noticeable in AD 3814 given the larger mass ratio in this system.

6.1.2. Distance to Praesepe

Literature distance estimates to Praesepe range from ∼160–190 pc, with the more recent determinations clustering around ∼175–185 pc (Mermilliod et al. 1990; Reglero & Fabregat 1991; Gatewood & de Jonge 1994; Percival et al. 2003; An et al. 2007; van Leeuwen 2009; Gaia Collaboration et al. 2017). *Gaia* DR1 parallaxes imply a distance of $182.8 \pm 1.7 \pm 14$ (the two uncertainties are the error on the cluster center determination and the observed spread of cluster members on the sky; Gaia Collaboration et al. 2017). Our distance estimates for ADs 3814, 2615, and 1508 are $170.4^{+11.0}_{-8.9}$, 179^{+13}_{-10}, and 166^{+25}_{-23} pc, respectively, which are all in agreement with the *Gaia* parallax distance. As AD 3116 is single lined, we do not have precise radii and surface gravities, so we placed a prior on the distance to the system of $d_{\rm sys} = 182.8 \pm 14$ pc, and hence do not quote a distance for this system as we essentially recover our prior.

Empirical bolometric corrections (BCs) are available for M-dwarfs (e.g., Mann et al. 2015). Combining these with our calculated radii gives the system bolometric flux, which can be converted to absolute bandpass magnitudes using the derived BCs and compared to apparent magnitudes to estimate the distance using the distance modulus (see the M15 distances in Table 5). We note that these are also in agreement with both our distances and the *Gaia* cluster value.

6.2. Comparison with Stellar Evolution Models

6.2.1. The Newly Characterized EBs

With precise masses, radii, and effective temperatures for both stars in ADs 3814 and 2615, we can test the predictions of stellar evolution theory for low-mass stars at the beginning of the main-sequence phase of evolution. Figure 21 compares the fundamental parameters of ADs 3814 and 2615 to the PARSEC v1.2 (Bressan et al. 2012; Chen et al. 2014) and BHAC15 (Baraffe et al. 2015) models. Praesepe is slightly metal rich ($[{\rm Fe/H}] \approx 0.14$), but the closest BHAC15 models in metallicity have solar composition. Therefore, we compare our results with both the solar metallicity PARSEC and BHAC15 models (Figure 21 top row) and also compare to the PARSEC models at Praesepe metallicity (Figure 21 bottom row). In the mass–radius plane (left panels), the PARSEC models (solid lines) predict slightly larger radii than BHAC15 (dashed lines) for a given mass, but both models are able to explain the two components of each system with a single isochrone at the 1σ level (for PARSEC, this is true for both solar and Praesepe metallicities). This agreement is encouraging as the masses of AD 3814 are constrained to 2% for both components and the primary and secondary radii to 1% and 3%, respectively. The uncertainties on the masses and radii of AD 2615 are slightly larger, given that the system is fainter, and there are fewer eclipses and RVs, but the masses and radii are still both constrained to 6% for the primary and 5% for the secondary.

We note that both systems are young (sub-Gyr) and display modest Hα emission. Therefore, compared to old M-dwarfs, these Praesepe stars are expected to have relatively strong magnetic fields and high spot coverage. Higher activity levels are thought to result in stars with lower effective temperatures and inflated radii (e.g., Chabrier et al. 2007; MacDonald & Mullan 2014), and this is often seen in observations (e.g., Feiden & Chaboyer 2012). Stars in EBs with longer orbital periods appear to show better agreement with the models, but those that do show disagreement tend to be fully convective. This might suggest that for stars with radiative cores and convective outer envelopes, disagreements with models are driven by rotation and magnetic activity, but comparisons for

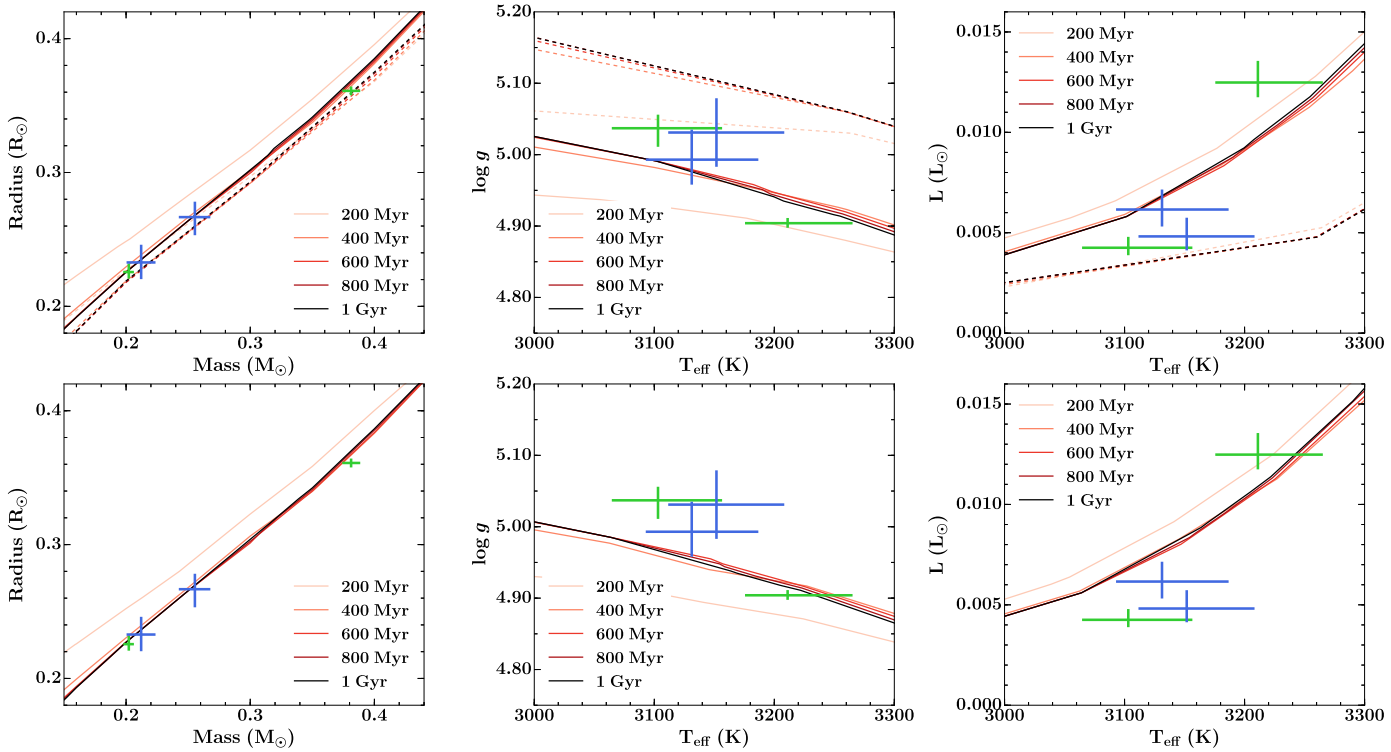

Figure 21. Comparison of the fundamental parameters of ADs 3814 and 2615 (green and blue, respectively) to the PARSEC v1.2 and BHAC15 model isochrones (solid and dashed lines, respectively). The top row shows the PARSEC (solid) and BHAC15 (dashed) models in the mass–radius, $T_{\rm eff}$–log g, and $T_{\rm eff}$–luminosity planes (left to right) at solar metallicity. The bottom row shows the same planes but for the PARSEC models at the metallicity of Praesepe ($Z = 0.0174$). The model isochrones shown are common in all plots and range from 200 Myr (lightest) to 1 Gyr (darkest).

fully convective stars are subject to other errors (Feiden 2015). That these two fully (or almost fully) convective EB systems are active and have relatively short (6–12 day) periods yet agree well with the radius predictions of non-magnetic models presents a further challenge to stellar evolution theory.

Although the masses and radii appear to be in agreement, including $T_{\rm eff}$ complicates the picture. We next compare our results in the $T_{\rm eff}$–log g plane. The surface gravity, log g, combines the mass and radius information, which agree well for both models, and hence this parameter should also be well explained. In the middle column of Figure 21, we see significant discrepancies between the data and models, which point toward problems in the model $T_{\rm eff}$ scales. The models substantially diverge in their $T_{\rm eff}$ predictions, with the BHAC15 models being hotter by ∼200–250 K across the mid-M-dwarf range, and the PARSEC models being perhaps 10–25 K cooler than the data. We note that this is also seen in the mass–$T_{\rm eff}$ and radius–$T_{\rm eff}$ planes (not shown here). Both sets of models essentially predict the same $T_{\rm eff}$ independent of age for $t \gtrsim 400$ Myr out to 10 Gyr. Our SED analysis yields $T_{\rm eff}$ values that are in closer agreement to the PARSEC models than BHAC15, but both models predict a steeper $T_{\rm eff}$ scale than the data suggest (note that a steeper model $T_{\rm eff}$ scale manifests as a shallower gradient in $T_{\rm eff}$–log g space, as observed). One option is that the model $T_{\rm eff}$ scales are too steep for mid-M-dwarfs but it could also be that additional phenomena, not included in the models, are responsible for the observed slope difference. Both ADs 3814 and 2615 display starspot modulation in the *K2* light curves. As neither PARSEC nor BHAC15 includes the effect of magnetic fields and starspots, it could be that some of the discrepancy arises from these phenomena rather than the model $T_{\rm eff}$ scale being too steep per se.

Although the primary component of AD 3814 agrees with the PARSEC Praesepe metallicity models, the secondary lies above the relation. We can take the primary star as an example to explore the required spot coverage and contrast ratio needed to bring its computed $T_{\rm eff}$ onto the same expected isochrone as the secondary component. We note that this scenario would require the PARSEC $T_{\rm eff}$ scale to be underpredicting the true unspotted $T_{\rm eff}$, but this is plausible so we continue with the exercise nonetheless. Assuming a spotted-to-unspotted photospheric temperature ratio of 0.8 (e.g., Grankin 1998) would require ∼25% spot coverage. To bring the primary and secondary components within 1σ would only require a 10% spot coverage on the primary. We note, however, that the radius posterior medians sit just below the zero age main sequence predicted by the PARSEC models and invoking starspots to redress the $T_{\rm eff}$ slope differences would imply a corresponding decrease in the radii for these stars without spots.

To bring the primary and secondary components of AD 3814 into agreement with the BHAC15 models would require spot coverages of 30%–40% on each star. While high, this is consistent with observations of active late-type stars, especially those in close binaries (e.g., O'Neal et al. 2004). We note that the BHAC15 models track a steeper path in log g–$T_{\rm eff}$ space beyond 3400 K (corresponding to a shallower $T_{\rm eff}$ scale). Simply shifting the BHAC15 models cooler by 250 K would bring them into agreement with all four stars. This is not

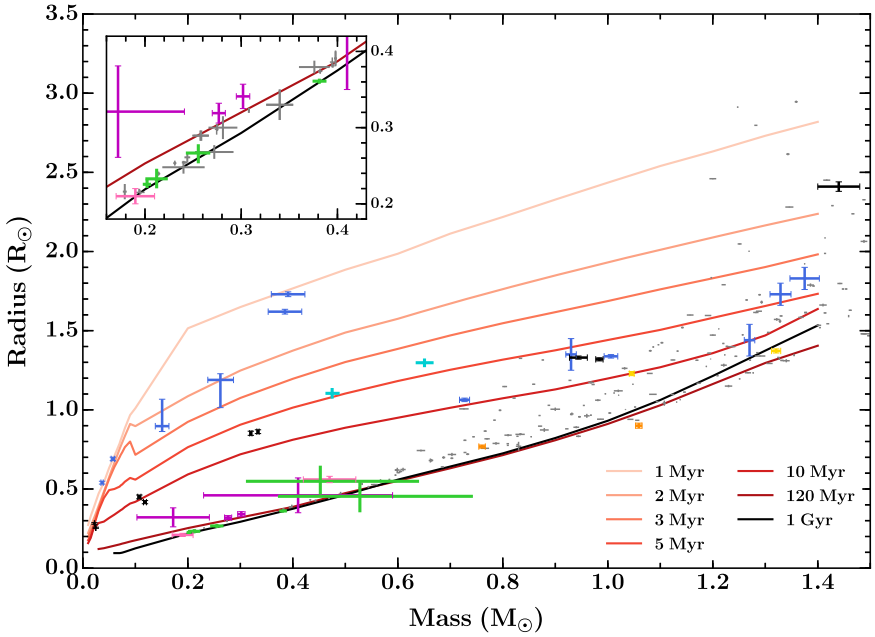

Figure 22. Mass–radius relation for detached double-lined eclipsing binaries (EBs) below 1.5 $M_\odot$. Data compiled from Table 5 and DEBCat (Southworth 2015). EBs that are members of open clusters are colored while field EBs are shown in gray. The clusters containing well-characterized EBs are Orion (blue), Upper Scorpius (black), NGC 2264 (cyan), Pleiades (magenta), Hyades (orange), NGC 1647 (pink), Per OB2 (gold), and the new Praesepe EBs (green) presented here. The colored lines represent the solar metallicity isochrones of Baraffe et al. (2015) from 1 Myr to 1 Gyr (top to bottom). The inset (top left) is a zoom on the region containing ADs 3814 and 2615 to allow a closer comparison between the models and current observational constraints for low-mass stars. Here we also include the compilation of known low-mass EBs presented in Dittmann et al. (2017).

possible with the PARSEC models, so it remains a valid option that the PARSEC model temperature scale is too steep over the mass range probed (∼0.2–0.4 $M_\odot$). However, more precisely characterized M-dwarf binaries are required to confirm this tentative statement.

The radii and effective temperatures combine to determine the luminosity of a star. Stellar evolution models are typically found to underpredict the radii and overpredict the effective temperatures of active low-mass stars; however, these combine to essentially recover the correct luminosity. The right column of Figure 21, shows the radiative $T_{\rm eff}$–luminosity relation. As expected, the BHAC15 models appear to underpredict the luminosity because the model $T_{\rm eff}$ is too high. The PARSEC models are in better agreement: they are able to follow the general trend of the data and explain the primary component of AD 3814 and the secondary of AD 2615, but the other components are slightly discrepant at the $\sim 1.5\sigma$ level.

6.2.2. Updated Mass–Radius Relation for Low-mass EBs

Figure 22, shows the mass–radius relation for detached double-lined EBs below $M < 1.5\,M_\odot$. Field EBs are shown in gray while members of young open clusters—including our newly discovered systems reported here—are colored by cluster (see figure caption for color scheme). The fundamental parameters of the known cluster EBs with both components below 1.5 $M_\odot$ are reported in Table 6. The three double-lined Praesepe systems reported here make a significant contribution to known cluster EBs, increasing the total number below 1.5 $M_\odot$ by almost 20% (and increasing the known double-lined M-dwarf EB population by 30%). Furthermore, ADs 3814 and 2615 add precise constraints for stellar evolution models at the zero-to-early age main sequence for low-mass stars.

6.2.3. Age of Praesepe

As briefly discussed in the introduction, the age of Praesepe has been debated in recent years. It has typically been estimated at ∼600–650 Myr by isochrone fitting, often through association with the Hyades (e.g., Perryman et al. 1998; Salaris et al. 2004; Fossati et al. 2008). However, Brandt & Huang (2015b) found that including rotation in stellar models implied an age of 790 ± 60 Myr (2σ uncertainty) for Praesepe, which is in agreement with their Hyades age of ∼750–800 Myr (Brandt & Huang 2015a). This older age estimate arises from the fact that rotation results in longer main-sequence lifetimes and hence older ages for post-turnoff populations. This result was corroborated by David & Hillenbrand (2015), who also include the effect of stellar rotation in their comparison between stellar atmospheric parameters (derived from Strömgren photometry) and theoretical isochrones.

Somewhat orthogonal to the ages inferred from radiative properties such as L and T, the ages of EB systems can be determined through comparison of their masses and radii with stellar evolution models (see Section 6.2.1). Unfortunately, over the mass range probed by our EBs, the several hundred Myr Praesepe sits roughly at the zero age main sequence. As M-dwarf evolution is slow, their increase in radius as they evolve through their first several Gyr on the main sequence is correspondingly small. Therefore, using our masses and radii to independently estimate the age of Praesepe would carry significant uncertainty and would not provide useful input to the current 600 Myr versus 800 Myr age discussion.

6.3. Circularization and Synchronization

6.3.1. Tidal Circularization

In this section, we compare our findings for the new EB systems to the expectations for tidal circularization and spin–

Table 6
Published Double-lined Eclipsing Binary Systems in Sub-Gyr Open Clusters where Both Components are Below 1.5 $M_{\odot}$, Ordered by Ascending Primary Mass

Name	M_{pri} ($M_{\odot}$)	M_{sec} ($M_{\odot}$)	R_{pri} ($R_{\odot}$)	R_{sec} ($R_{\odot}$)	Cluster[a]	Age (Myr)	Year	References
EPIC 203868608	0.02216 ± 0.00045	0.02462 ± 0.00055	0.2823 ± 0.0051	0.2551 ± 0.0036	Upper Sco	5–10	2016	(1)
2MJ0535-05	0.0572 ± 0.0033	0.0366 ± 0.0022	0.690 ± 0.011	0.540 ± 0.009	ONC	1–2	2006	(2), (3)
EPIC 203710387	0.1183 ± 0.0028	0.1076 ± 0.0031	0.417 ± 0.010	0.450 ± 0.012	Upper Sco	5–10	2015	(4), (1)
JW 380	0.262 ± 0.025	0.151 ± 0.013	1.189 ± 0.175	0.897 ± 0.170	ONC	1–2	2007	(5)
HCG 76	0.3019 ± 0.0070	0.2767 ± 0.0068	0.341 ± 0.016	0.319 ± 0.013	Pleiades	125	2016	(6)
USco CTIO 5	0.3336 ± 0.0022	0.3200 ± 0.0022	0.862 ± 0.012	0.852 ± 0.013	Upper Sco	5–10	2015	(7), (1)
Par 1802	0.391 ± 0.032	0.385 ± 0.032	1.73 ± 0.02	1.62 ± 0.02	ONC	1–2	2008	(8)–(10)
MHO 9	0.41 ± 0.18	0.172 ± 0.069	0.46 ± 0.11	0.321 ± 0.060	Pleiades	125	2016	(6)
2MJ0446+19	0.47 ± 0.05	0.19 ± 0.02	0.56 ± 0.02	0.21 ± 0.01	NGC 1647	150	2006	(11)
CoRoT 223992193	0.668 ± 0.012	0.4953 ± 0.0073	1.295 ± 0.040	1.107 ± 0.050	NGC 2264	3–6	2014	(12)
HD 144548	0.984 ± 0.007	0.944 ± 0.017	1.319 ± 0.010	1.330 ± 0.010	Upper Sco	5–10	2015	(15)
	1.44 ± 0.04[b]		2.41 ± 0.03[b]					
MML 53	0.994 ± 0.030	0.857 ± 0.026	2.201 ± 0.071[c]		UCL	15	2010	(13), (14)
V1174 Ori	1.006 ± 0.013	0.7271 ± 0.0096	1.338 ± 0.011	1.063 ± 0.011	Ori OB 1c	5–10	2004	(16)
V818 Tau	1.0591 ± 0.0062	0.7605 ± 0.0062	0.900 ± 0.016	0.768 ± 0.010	Hyades	600–800	2002	(17)
RXJ 0529.4+0041A	1.27 ± 0.01	0.93 ± 0.01	1.44 ± 0.10	1.35 ± 0.10	Ori OB 1a	7–13	2000	(18)–(20)
NP Per	1.3207 ± 0.0087	1.0456 ± 0.0046	1.372 ± 0.013	1.229 ± 0.013	Per OB 2	6–15	2016	(21)
ASAS J0528+03	1.375 ± 0.028	1.329 ± 0.020	1.83 ± 0.07	1.73 ± 0.07	Ori OB 1a	7–13	2008	(22)
Praesepe Systems Published in This Paper								
AD 3814	0.3813 ± 0.0074	0.2022 ± 0.0045	0.3610 ± 0.0033	0.2256 ± 0.0063	Praesepe	600–800	2017	this work
AD 2615	0.212 ± 0.012	0.255 ± 0.013	0.233 ± 0.013	0.267 ± 0.014	Praesepe	600–800	2017	this work
AD 1508	0.45 ± 0.19	0.53 ± 0.22	0.549 ± 0.099	0.45 ± 0.10	Praesepe	600–800	2017	this work

Notes. Where asymmetric error bars were reported in the original papers, we quote the larger of the two here. In some instances we quote larger uncertainties than the discovery papers report, following Stassun et al. (2014).
[a] ONC = Orion Nebula Cluster; UCL = Upper Centaurus Lupus; Upper Sco = Upper Scorpius.
[b] Tertiary component that is also eclipsed.
[c] Radius sum (individual radii have not been determined).
References. (1) David et al. (2016b); (2) Stassun et al. (2006); (3) Stassun et al. (2007); (4) Lodieu et al. (2015); (5) Irwin et al. (2007); (6) David et al. (2016a); (7) Kraus et al. (2015); (8) Cargile et al. (2008); (9) Stassun et al. (2008); (10) Gómez Maqueo Chew et al. (2012); (11) Hebb et al. (2006); (12) Gillen et al. (2014) (13) Hebb et al. (2010); (14) Hebb et al. (2011); (15) Alonso et al. (2015); (16) Stassun et al. (2004); (17) Torres & Ribas (2002); (18) Covino et al. (2000); (19) Covino et al. (2001); (20) Covino et al. (2004); (21) Lacy et al. (2016); (22) Stempels et al. (2008).

orbit synchronization at the age of Praesepe. The binaries presented here are particularly valuable benchmarks for studies of tidal dissipation timescales in close binaries, as they are at or near the beginning of their main-sequence evolution. Zahn & Bouchet (1989) posited that essentially all tidal circularization should occur during the PMS phase, when stars are larger and have deeper convective envelopes. If this theory were correct, all late-type main-sequence binaries with periods less than ∼8 days should be circularized. Binaries with longer orbital periods would retain their primordial eccentricities and experience negligible tidal circularization after the PMS phase.

However, Meibom & Mathieu (2005) used observations of binaries in coeval stellar populations to clearly show that tidal dissipation proceeds to circularize orbits well after the PMS stage (see their Figure 9). Although standard equilibrium tide theory (Zahn 1989; Claret & Cunha 1997) and dynamical tide theory (Witte & Savonije 2002) do predict exactly this trend, binaries are generally observed to circularize more quickly than theory predicts (i.e., tidal dissipation is a more efficient process than expected). The binary population of Praesepe and the Hyades is a conspicuous outlier to this trend, indicating agreement with theory but significant tension with observations of all other well-characterized clusters. However, Zahn & Bouchet (1989) cautioned that two short-period eccentric binaries in Praesepe and Hyades (KW 181 and VB 121) are single-lined systems, in which the secondaries could possibly be white dwarfs, meaning that the standard theory of tidal dissipation would not apply. Ignoring these two systems, those authors estimated binaries with periods below 8.5–11.9 days should be circularized by the age of the Hyades and, by extension, Praesepe. Our findings for AD 3814 and AD 2615 corroborate the notion that the circularization period for Praesepe is larger than previously measured, and to our knowledge AD 2615 is the longest period circular binary in either Praesepe or the Hyades. Revisiting the analysis of Meibom & Mathieu (2005) including these two systems would bring the observations for Praesepe into better agreement with those of other clusters, in the sense that binaries of a given age are observed to be circular out to longer periods than theory predicts.

As for AD 3116, tidal dissipation proceeds differently for extreme mass ratio systems (Ogilvie 2014), and so we caution against drawing conclusions based on its relatively high eccentricity ($e = 0.15$) given its short orbital period of <2 days. In fact, the recently discovered transiting brown dwarf in the significantly older Ruprecht 147 cluster similarly exhibits a relatively high eccentricity and short orbital period (Nowak et al. 2017).

Finally, we note that the transition between circular and eccentric binaries in a coeval stellar population (as demarcated either by the "cutoff period," i.e., the longest period circular binary, or preferably the "tidal circularization period") can in

principle be used to estimate the age of the stellar population (Mathieu & Mazeh 1988). Given sufficient data and a well-calibrated relation among clusters, the method could also be extended to close binaries in the field to provide an upper limit in age if the binary is eccentric, or a lower limit if it is circular.

6.3.2. Spin–Orbit Synchronization

The theoretical outcome of tidal evolution within a binary system is a circular orbit and a state of double synchronous rotation with the spin axes aligned to the orbital angular momentum vector. However, as noted by Ogilvie (2014), this theoretical prediction has never been observationally verified for a binary star system. This is in part due to the difficulty of measuring stellar rotation, particularly for both components of a binary, and the need for an eclipsing system to precisely measure obliquities.

Binaries for which the rotation period of one or more component can be measured, particularly within coeval stellar populations, are thus critical benchmarks for tidal synchronization studies. For the four binaries discussed here, one appears to be nearly synchronized (AD 1508), while the other three appear to be rotating subsynchronously (i.e., at a frequency lower than the orbital frequency). This observation is based on the measured $P_{\rm spot}/P_{\rm orb}$ ratios of 1.25, 1.08, and 1.14 for ADs 3814, 2615, and 3116, respectively. On the surface, this is surprising given that (1) the expected synchronization timescales are much smaller than the cluster age, and (2) tidal synchronization is expected to occur more quickly than circularization in close binaries (Zahn 1977; Hut 1981) and two of the subsynchronous binaries are on nearly circular orbits (ADs 3814 and 2615).

It is important to note that photometric variations indicate a star's surface rotation rate, but the spin of the interior layers is not measured and known only to the extent to which there is reason to believe the interior is coupled to the surface. For the binaries with mass ratios near unity, both stars are contributing to the observed brightness modulations, but in the absence of multiple distinct peaks in a periodogram, we infer the modulation period to indicate the rotation of the primary. Notably, surface differential rotation can lead to configurations in which the spin of the equatorial regions is synchronized with the orbit while higher latitudes may be rotating more slowly. Such a scenario has been suggested to explain observations of the late-type EB H II 2407 in the Pleiades (David et al. 2015). Indeed, there is observational evidence (Barnes et al. 2015) and theoretical motivation (Schuessler & Solanki 1992; Granzer et al. 2000) for polar spots on rapidly rotating, fully convective stars.

However, unlike the Pleiades EB, the binaries presented here exhibit much larger discrepancies between the rotation and orbital periods. The measured rates of differential rotation have been observed to decrease strongly with stellar temperature (Barnes et al. 2005; Collier Cameron 2007). Using the empirical formula of Collier Cameron (2007), the expected rates of differential rotation for the stars considered here are all below 10^{-3} rad day^{-1}. If we assume that the orbits are synchronized at the equator and that polar spots are responsible for the measured rotation periods, then the implied rates of differential rotation for ADs 3814, 2615, and 3116 would be 0.21, 0.04, and 0.38 rad day^{-1}, respectively. These values are significantly higher than the differential rotation rates measured for fully convective stars (Morin et al. 2008; Reinhold et al. 2013; Davenport et al. 2015). Our observations therefore indicate either: (1) tidal synchronization proceeds more slowly in fully convective stars than the theory of equilibrium tides predicts, (2) magnetic braking is currently playing a more important role in the spin evolution of these binaries than tidal forces, or (3) differential rotation in fully convective stars can be much more important than previously appreciated. We consider the last explanation to be the least plausible.

Subsynchronous rotation has previously been observed for short-period binaries in the younger M35 and M34 clusters, aged ∼150 Myr and ∼250 Myr, respectively (Meibom et al. 2006). As those authors noted, this result is in direct contradiction with expectations of tidal evolution on the main sequence, which predicts binaries with periods near or below the circularization period (which AD 3814 and AD 2615 apparently are) to be rotating pseudosynchronously (synchronized with the instantaneous orbital angular velocity at periastron) or slightly *supersynchronous*.

We conclude by noting that current theories of tidal evolution carry significant and underexplored uncertainties. In particular, theory for solar-type and early-type stars is more developed than that for fully convective stars. Tidal dissipation is expected to be more efficient, and thus circularization more rapid, in stars with convective outer layers (Zahn 1975), which is supported observationally (Van Eylen et al. 2016).

7. Conclusions

We presented photometric time series data from *Kepler*/*K2* and follow-up high-dispersion spectroscopy from Keck/HIRES in order to characterize four new EB systems in the sub-Gyr old Praesepe cluster. These new discoveries increase the number of characterized EBs below 1.5 $M_{\odot}$ in sub-Gyr open clusters by 20%, and add 40% to the cluster EB population with masses $M \lesssim 0.6\,M_{\odot}$.

We analyze these low-mass EBs with GP–EBOP, a new multi-purpose Gaussian process EB and transiting exoplanet model, to determine model-independent stellar masses and radii. We present an updated method of simultaneously determining the effective temperatures of both stars as well as the distance to an EB by modeling the system's SED. This approach capitalizes on the posterior constraints from the joint light curve and RV modeling to break existing degeneracies and also correctly interprets the light curve model's band-specific surface brightness ratio, rather than using it to approximate an effective temperature ratio.

We determine the masses of AD 3814 to 2% precision and the primary and secondary radii to 1% and 3%, respectively. The masses and radii of AD 2615 are both determined to 6% precision for the primary and to 5% for the secondary. Together with effective temperatures determined to a typical precision of ±50 K, we test the PARSEC v1.2 and BHAC15 stellar evolution models. Overall, the EB parameters are most consistent with the PARSEC models, primarily because the BHAC15 temperature scale is too hot over the mass–age range probed. Both the PARSEC and BHAC15 models are able to explain the masses and radii of ADs 3814 and 2615 with a single isochrone in the range ∼400–1000 Myr, but predicting $T_{\rm eff}$ proves more challenging. Our SED-derived $T_{\rm eff}$ values, which are consistent with those derived from empirical M-dwarf relations, are better matched to the PARSEC models. We find that the BHAC15 models predict temperatures $T_{\rm eff}$ ∼100–300 K hotter than our data, whereas the PARSEC

models lie in the correct $T_{\rm eff}$ range. However, both models predict a steeper $T_{\rm eff}$ track over the mass range $M \sim 0.2$–0.4 $M_{\odot}$ than our data suggest. More M-dwarf EBs with precise $T_{\rm eff}$ values on the main sequence are required to confirm this tentative statement. Our luminosities are in agreement with the PARSEC model predictions, but we find that the BHAC15 models overpredict this parameter primarily due to their high $T_{\rm eff}$ values. Although both ADs 3814 and 2615 possess precise solutions, we note that AD 3814 would benefit from a more detailed modeling of the individual eclipses (especially incorporating a full starspot model), and AD 2615 would benefit from additional RVs to tighten the existing solution.

We present a preliminary solution for a third detached double-lined system, AD 1508. The *K2* light curve displays clear, but shallow, eclipses on both stars, and the three Keck/HIRES RVs we obtained show the two stars not to be rapid rotators. This system is therefore amenable to precise characterization but would require further RV measurements throughout the orbital phase and may also benefit from targeted eclipse monitoring with moderate-aperture ground-based telescopes.

The final system, AD 3116, comprises a mid-M-dwarf primary star with a transiting brown dwarf companion ($M \sim 54$ $M_{\rm Jup}$). There are only ∼20 transiting brown dwarf systems known: AD 3116 is one of only three systems where the primary is an M-dwarf, and is only the second transiting brown dwarf system discovered in an open cluster (and the first younger than a Gyr). It will therefore be a favorable target for future transiting brown dwarf studies.

Finally, we find that ADs 3814 and 2615, which have orbital periods of 6.0 and 11.6 days, are circularized but not synchronized, with at least one component rotating subsynchronously. This contradicts the expectations of tidal evolution, which would predict synchronization to proceed faster than circularization in these systems and for it to have been achieved by the age of Praesepe. Our observations therefore suggest that either tidal synchronization proceeds more slowly in fully convective stars than the theory of equilibrium tides predicts, or magnetic braking is currently playing a more important role in the spin evolution of these binaries than tidal forces.

We thank Pierre Maxted for interesting discussions and John Southworth for help compiling Table 6. This paper includes data collected by the *Kepler*/*K2* mission. Funding for the *K2* mission of *Kepler* is provided by the NASA Science Mission directorate. Some of the data presented in this paper were obtained from the Mikulski Archive for Space Telescopes (MAST) under support by the NASA Office of Space Science via grant NNX09AF08G and by other grants and contracts. Some of the data presented herein were obtained at the W. M. Keck Observatory, which is operated as a scientific partnership among the California Institute of Technology, the University of California, and the National Aeronautics and Space Administration. The Observatory was made possible by the generous financial support of the W. M. Keck Foundation. The authors wish to recognize and acknowledge the very significant cultural role and reverence that the summit of Maunakea has always had within the indigenous Hawaiian community. We are most fortunate to have the opportunity to conduct observations from this mountain. Finally, we would like to thank the anonymous referee for their careful reading of the manuscript and helpful suggestions for improvement.

Facilities: Kepler (*K2*), Keck:I, Sloan, CTIO:2MASS, FLWO:2MASS, *WISE*.

Software: astropy (Astropy Collaboration et al. 2013), `emcee` (Foreman-Mackey et al. 2013), `george` (Ambikasaran et al. 2014).

Note added in proof. We note that AD 3814 has been contemporaneously analyzed by Kraus et al. (2017). In addition, it has been pointed out to us that AD 2615 and AD 3116 appear in the online tables of Libralato et al. (2016) as "candidate variables," with a period reported therein for AD 3116 essentially equivalent to the EB period reported here.

ORCID iDs

Edward Gillen https://orcid.org/0000-0003-2851-3070
Trevor J. David https://orcid.org/0000-0001-6534-6246
Suzanne Aigrain https://orcid.org/0000-0003-1453-0574
Luisa Rebull https://orcid.org/0000-0001-6381-515X
John Stauffer https://orcid.org/0000-0003-3595-7382
Ann Marie Cody https://orcid.org/0000-0002-3656-6706
Didier Queloz https://orcid.org/0000-0002-3012-0316

References

Adams, J. D., Stauffer, J. R., Skrutskie, M. F., et al. 2002, AJ, 124, 1570
Aigrain, S., Hodgkin, S., Irwin, J., et al. 2007, MNRAS, 375, 29
Aigrain, S., Parviainen, H., & Pope, B. J. S. 2016, MNRAS, 459, 2408
Aigrain, S., Pont, F., & Zucker, S. 2012, MNRAS, 419, 3147
Alencar, S. H. P., & Vaz, L. P. R. 1997, A&A, 326, 257
Allard, F., Homeier, D., & Freytag, B. 2012, RSPTA, 370, 2765
Alonso, R., Deeg, H. J., Hoyer, S., et al. 2015, A&A, 584, L8
Ambikasaran, S., Foreman-Mackey, D., Greengard, L., Hogg, D. W., & O'Neil, M. 2014, arXiv:1403.6015
An, D., Terndrup, D. M., Pinsonneault, M. H., et al. 2007, ApJ, 655, 233
Astropy Collaboration, Robitaille, T. P., Tollerud, E. J., et al. 2013, A&A, 558, A33
Baker, D. E. A., Jameson, R. F., Casewell, S. L., et al. 2010, MNRAS, 408, 2457
Baraffe, I., Homeier, D., Allard, F., & Chabrier, G. 2015, A&A, 577, A42
Barnes, J. R., Collier Cameron, A., Donati, J.-F., et al. 2005, MNRAS, 357, L1
Barnes, J. R., Jeffers, S. V., Jones, H. R. A., et al. 2015, ApJ, 812, 42
Bate, M. R. 2009, MNRAS, 392, 590
Bayliss, D., Hojjatpanah, S., Santerne, A., et al. 2017, AJ, 153, 15
Benedict, G. F., Henry, T. J., Franz, O. G., et al. 2016, AJ, 152, 141
Boesgaard, A. M., Roper, B. W., & Lum, M. G. 2013, ApJ, 775, 58
Boudreault, S., Lodieu, N., Deacon, N. R., & Hambly, N. C. 2012, MNRAS, 426, 3419
Brandt, T. D., & Huang, C. X. 2015a, ApJ, 807, 58
Brandt, T. D., & Huang, C. X. 2015b, ApJ, 807, 24
Bressan, A., Marigo, P., Girardi, L., et al. 2012, MNRAS, 427, 127
Cargile, P. A., Stassun, K. G., & Mathieu, R. D. 2008, ApJ, 674, 329
Chabrier, G., Gallardo, J., & Baraffe, I. 2007, A&A, 472, L17
Chen, Y., Girardi, L., Bressan, A., et al. 2014, MNRAS, 444, 2525
Claret, A., & Cunha, N. C. S. 1997, A&A, 318, 187
Claret, A., Hauschildt, P. H., & Witte, S. 2012, A&A, 546, A14
Collier Cameron, A. 2007, AN, 328, 1030
Covino, E., Catalano, S., Frasca, A., et al. 2000, A&A, 361, L49
Covino, E., Frasca, A., Alcalá, J. M., Paladino, R., & Sterzik, M. F. 2004, A&A, 427, 637
Covino, E., Melo, C., Alcalá, J. M., et al. 2001, A&A, 375, 130
Csizmadia, S. 2016, in The CoRoT Legacy Book, ed. A. Baglin (Les Ulis: EDP), 143
Czekala, I., Andrews, S. M., Mandel, K. S., Hogg, D. W., & Green, G. M. 2015, ApJ, 812, 128
Czekala, I., Mandel, K. S., Andrews, S. M., et al. 2017, ApJ, 840, 49
Davenport, J. R. A., Hebb, L., & Hawley, S. L. 2015, ApJ, 806, 212
David, T. J., Conroy, K. E., Hillenbrand, L. A., et al. 2016a, AJ, 151, 112
David, T. J., & Hillenbrand, L. A. 2015, ApJ, 804, 146
David, T. J., Hillenbrand, L. A., Cody, A. M., Carpenter, J. M., & Howard, A. W. 2016b, ApJ, 816, 21
David, T. J., Stauffer, J., Hillenbrand, L. A., et al. 2015, ApJ, 814, 62

Dittmann, J. A., Irwin, J. M., Charbonneau, D., et al. 2017, ApJ, 836, 124
Feiden, G. A. 2015, in ASP Conf. Ser. 496, Living Together: Planets, Host Stars and Binaries, ed. S. M. Rucinski, G. Torres, & M. Zejda (San Francisco, CA: ASP), 137
Feiden, G. A., & Chaboyer, B. 2012, ApJ, 757, 42
Foreman-Mackey, D., Hogg, D. W., Lang, D., & Goodman, J. 2013, PASP, 125, 306
Fossati, L., Bagnulo, S., Landstreet, J., et al. 2008, A&A, 483, 891
Gaia Collaboration, van Leeuwen, F., Vallenari, A., et al. 2017, A&A, 601, A19
Gatewood, G., & de Jonge, J. K. 1994, ApJ, 428, 166
Gillen, E., Aigrain, S., McQuillan, A., et al. 2014, A&A, 562, A50
Gómez Maqueo Chew, Y., Stassun, K., Prša, A., et al. 2012, ApJ, 745, 58
Grankin, K. N. 1998, AstL, 24, 497
Granzer, T., Schüssler, M., Caligari, P., & Strassmeier, K. G. 2000, A&A, 355, 1087
Hambly, N. C., Steele, I. A., Hawkins, M. R. S., & Jameson, R. F. 1995, A&AS, 109, 29
Hebb, L., Cegla, H. M., Stassun, K. G., et al. 2011, A&A, 531, A61
Hebb, L., Stempels, H. C., Aigrain, S., et al. 2010, A&A, 522, A37
Hebb, L., Wyse, R. F. G., Gilmore, G., & Holtzman, J. 2006, AJ, 131, 555
Howell, S. B., Sobeck, C., Haas, M., et al. 2014, PASP, 126, 398
Husser, T.-O., Wende-von Berg, S., Dreizler, S., et al. 2013, A&A, 553, A6
Hut, P. 1981, A&A, 99, 126
Irwin, J., Aigrain, S., Hodgkin, S., et al. 2007, MNRAS, 380, 541
Irwin, J. M., Quinn, S. N., Berta, Z. K., et al. 2011, ApJ, 742, 123
Jones, B. F., & Cudworth, K. 1983, AJ, 88, 215
Jones, B. F., & Stauffer, J. R. 1991, AJ, 102, 1080
Kafka, S., & Honeycutt, R. K. 2006, AJ, 132, 1517
Khalaj, P., & Baumgardt, H. 2013, MNRAS, 434, 3236
Kipping, D. M. 2013, MNRAS, 435, 2152
Klein Wassink, W. J. 1927, PGro, 41, 1
Kraus, A. L., Cody, A. M., Covey, K. R., et al. 2015, ApJ, 807, 3
Kraus, A. L., Douglas, S. T., Mann, A. W., et al. 2017, ApJ, 845, 72
Kraus, A. L., & Hillenbrand, L. A. 2007, AJ, 134, 2340
Lacy, C. H. S., Fekel, F. C., Pavlovski, K., Torres, G., & Muterspaugh, M. W. 2016, AJ, 152, 2
Libralato, M., Nardiello, D., Bedin, L. R., et al. 2016, MNRAS, 463, 1780
Lodieu, N., Alonso, R., González Hernández, J. I., et al. 2015, A&A, 584, A128
Lucy, L. B. 1967, ZAp, 65, 89
MacDonald, J., & Mullan, D. J. 2014, ApJ, 787, 70
Mandel, K., & Agol, E. 2002, ApJL, 580, L171
Mann, A. W., Feiden, G. A., Gaidos, E., Boyajian, T., & von Braun, K. 2015, ApJ, 804, 64
Mathieu, R. D., & Mazeh, T. 1988, ApJ, 326, 256
Meibom, S., & Mathieu, R. D. 2005, ApJ, 620, 970
Meibom, S., Mathieu, R. D., & Stassun, K. G. 2006, ApJ, 653, 621
Mermilliod, J.-C., Weis, E. W., Duquennoy, A., & Mayor, M. 1990, A&A, 235, 114
Morales-Calderón, M., Stauffer, J. R., Stassun, K. G., et al. 2012, ApJ, 753, 149
Morin, J., Donati, J.-F., Petit, P., et al. 2008, MNRAS, 390, 567
Netopil, M., Paunzen, E., Heiter, U., & Soubiran, C. 2016, A&A, 585, A150
Neuhäuser, R., Errmann, R., Berndt, A., et al. 2011, AN, 332, 547
Nidever, D. L., Marcy, G. W., Butler, R. P., Fischer, D. A., & Vogt, S. S. 2002, ApJS, 141, 503
Nowak, G., Palle, E., Gandolfi, D., et al. 2017, AJ, 153, 131
Ogilvie, G. I. 2014, ARA&A, 52, 171
O'Neal, D., Neff, J. E., Saar, S. H., & Cuntz, M. 2004, AJ, 128, 1802
Pace, G., Pasquini, L., & François, P. 2008, A&A, 489, 403
Parviainen, H., & Aigrain, S. 2015, MNRAS, 453, 3821
Pecaut, M. J., & Mamajek, E. E. 2013, ApJS, 208, 9
Pepper, J., Gillen, E., Parviainen, H., et al. 2017, AJ, 153, 177
Percival, S. M., Salaris, M., & Kilkenny, D. 2003, A&A, 400, 541
Perryman, M. A. C., Brown, A. G. A., Lebreton, Y., et al. 1998, A&A, 331, 81
Pinfield, D. J., Dobbie, P. D., Jameson, R. F., et al. 2003, MNRAS, 342, 1241
Quinn, S. N., White, R. J., Latham, D. W., et al. 2012, ApJL, 756, L33
Rasmussen, C. E., & Williams, C. K. I. 2006, Gaussian Processes for Machine Learning (Cambridge, MA: MIT Press)
Rebull, L. M., Stauffer, J. R., Hillenbrand, L. A., et al. 2017, ApJ, 839, 92
Reglero, V., & Fabregat, J. 1991, A&AS, 90, 25
Reinhold, T., Reiners, A., & Basri, G. 2013, A&A, 560, A4
Roberts, S., Osborne, M., Ebden, M., et al. 2012, RSPTA, 371, 1984
Salaris, M., Weiss, A., & Percival, S. M. 2004, A&A, 414, 163
Schuessler, M., & Solanki, S. K. 1992, A&A, 264, L13
Sing, D. K. 2010, A&A, 510, A21
Southworth, J. 2015, in Proc. ASP Conf. Ser. 496, Living Together: Planets, Host Stars and Binaries, ed. S. M. Rucinski, G. Torres, & M. Zejda (San Francisco, CA: ASP), 164
Stassun, K. G., Feiden, G. A., & Torres, G. 2014, NewAR, 60, 1
Stassun, K. G., Mathieu, R. D., Cargile, P. A., et al. 2008, Natur, 453, 1079
Stassun, K. G., Mathieu, R. D., & Valenti, J. A. 2006, Natur, 440, 311
Stassun, K. G., Mathieu, R. D., & Valenti, J. A. 2007, ApJ, 664, 1154
Stassun, K. G., Mathieu, R. D., Vaz, L. P. R., Stroud, N., & Vrba, F. J. 2004, ApJS, 151, 357
Stauffer, J. 1982, PASP, 94, 678
Stempels, H. C., Hebb, L., Stassun, K. G., et al. 2008, A&A, 481, 747
Taylor, B. J. 2006, AJ, 132, 2453
Torres, G., Andersen, J., & Giménez, A. 2010, A&ARv, 18, 67
Torres, G., & Ribas, I. 2002, ApJ, 567, 1140
van Eyken, J. C., Ciardi, D. R., Rebull, L. M., et al. 2011, AJ, 142, 60
Van Eylen, V., Winn, J. N., & Albrecht, S. 2016, ApJ, 824, 15
van Leeuwen, F. 2009, A&A, 497, 209
Vogt, S. S., Allen, S. L., Bigelow, B. C., et al. 1994, Proc. SPIE, 2198, 362
Wang, P. F., Chen, W. P., Lin, C. C., et al. 2014, ApJ, 784, 57
West, A. A., Morgan, D. P., Bochanski, J. J., et al. 2011, AJ, 141, 97
Witte, M. G., & Savonije, G. J. 2002, A&A, 386, 222
Yang, X. L., Chen, Y. Q., & Zhao, G. 2015, AJ, 150, 158
Zahn, J.-P. 1975, A&A, 41, 329
Zahn, J.-P. 1977, A&A, 57, 383
Zahn, J.-P. 1989, A&A, 220, 112
Zahn, J.-P., & Bouchet, L. 1989, A&A, 223, 112